CHAPTER 2 : THE ORIFICE FLOW OF AQUEOUS AND ORGANIC FLEXIBLE POLYMER SOLUTIONS GOING FROM THE DILUTE TO THE CONCENTRATED RANGE.

Abstract.

Orifice flow is studied experimentally for solutions of flexible polymers. Previous work in our laboratory, in which flow parameters varied in the whole range, showed that for aqueous dilute high molecular weight polymer solutions this flow is characterized by three flow regimes. Each regime was interpreted in terms of distinct molecular effects governing tensile stress growth, by incorporating a particular structural model in a similarity analysis. The objectives of the present paper are to extend the validity of this model to solutions with organic solvents and to determine the different flow regimes when concentration is varied from the dilute to the concentrated range.

Results are presented for aqueous solutions of polyethylene oxide (concentrations from 10 ppm to 10%) for which concentration regimes were determined by shear rheometry and for two international workshop fluids based on polyisobutylene in organic solvents, the M1 (2440 ppm polymer) and A1 (2% polymer) fluids.

The flow regimes observed for the dilute solutions are the same as the ones already reported. For semi-dilute non-entangled solutions (1000ppm < c < 1% for polyethylene oxide and the M1 fluid), a further scaling is observed in the intermediate regime: P_g varies as q_v^4. This scaling is also predicted by our analysis, and is attributed to hydrodynamic interaction stresses that become dominant over elastic stresses as molecules unravel.

For entangled solutions (4% and 10% of PEO and the A1), a single smoother scaling is observed at stable flow. Extensional effects become less pronounced. This is attributed to the fact that entanglements limit both the rate and the extend of molecular deformation. For the pure PEO polymer, the flow curve has the form already found with other polymer melts.

The stability of the flow is also examined. The onset of small scale instabilities is observed at relatively low flow regimes. 3D unstable flow characterizes the high flow regimes. A non-dimensional representation where pressure drop is reduced by the one for an inelastic fluid and plotted as a function of the ratio of extensional to shear stress on the orifice plane, makes data collapse on a single curve for concentrated solutions.

$$\dot{\vec{d}} = L\,\vec{d} - \frac{f_s}{\tau_0}\vec{d} \qquad (2.2)$$

where η_s is the solvent viscosity, D the symmetric part of the velocity gradient tensor, and n the polymer number density. The quantity $(\mathbf{d}\otimes\mathbf{d})_{dev}$ denotes the deviatoric part of the tensor product of **d** by **d** and f_{el}, f_{int}, f_s are model coefficients. $\vec{d}$ accounts for molecular conformation and τ_0 is a time constant.

According to (eq. 2.1), the extra-stress tensor is the sum of three contributions: The solvent viscosity contribution, the chain elasticity and the hydrodynamic interaction among chains respectively. (Eq. 2.2) gives the evolution of $\vec{d}$ as a balance between hydrodynamic stretching exerted by the solvent and entropic elasticity of the molecules.

By a similarity analysis it was shown that [5, 6]:

- at low flow rates, there is little deformation of the molecules with respect to their rest state dimensions. In this case the solvent term of the stress tensor is dominant and the pressure drop varies linearly with the flow rate ($P_g \sim q_v$).
- at intermediate flow rates, the chain length may vary considerably with respect to the rest state length. In this case and in the absence of hydrodynamic interactions, the elastic term dominates over the solvent contribution and the pressure drop varies with the square of the flow rate ($P_g \sim q_v^2$). When the concentration reaches a value such that important hydrodynamic interaction occurs, the scaling becomes $P_g \sim q_v^4$. The important aspect of this regime is that molecules do not reach steady state in the upstream flow, since transit time is lower than the time needed for steady state stretching to be reached. So flow is governed by the transient elongational viscosity η_E^+.
- at high flow rates, molecules reach their fully stretched length. In the absence of hydrodynamic interaction $P_g \sim q_v^{\delta}$, where $\delta = q/(q+h) < 1$ (q and h are phenomenological constants). When hydrodynamic interaction occurs (more concentrated systems), $P_g \sim q_v$.

Experiments with dilute polyacrylamide solutions have shown the existence of the slopes 1 and 2 at the flow curve as a consequence of the dominance of the solvent and the elastic terms respectively, as well as of the slope 1 at high regimes which results from the dominance of the hydrodynamic interaction term [4]. For polyoxyethylene solutions evidence existed previously only for the first two slopes for concentrations till 500 ppm in the same study. In the present study we present experiments at a much higher concentration range in the whole range of the flow parameters. Evidence of the slope 1 which corresponds to the hydrodynamic interaction regime is given for solutions of polyoxyethylene and of the slope 4 which indicates hydrodynamic interaction during the unraveling of the chains when concentrations in the semi-dilute regime are used (2000 and 5000 ppm). The same flow pattern is shown for the M1 solution.

2.3. Rheometry.

2.3.1. Working fluids

Solutions of various concentrations of polyoxyethylene were tested, as well as two international standard solutions based on polyisobutylene.

The polyoxyethylene is available in powder form (Polyox WSR-301, Union Carbide Corporation, reported Mw of 4.10^6). Being immiscible with solvents such as glucose and glycerol, a sugar (Sacharose Rectapur-Sodipro France) - water mixture was used as a solvent (53/47 %w.). The concentration covered the range from 10 ppm to 10%. Experiments were also performed with the polymer melt at a temperature of 100°C in order to examine qualitative aspects at the upper limit of the concentration range.

For low concentrations, solutions were prepared in the following way : Polymer was first dissolved in demineralized water, approximately 5 times the final concentration. The initial solution was then gently stirred for two hours. The resulting optically clear fluid, was stored for 24 hours, and again stirred for 1 hour. It was then gradually poured to a mixture appropriate in order to result to a final sugar/water proportion of 53/47 in weight, and stirred for 24 hours. Each time moderate amounts were prepared (approximately 1 liter). In all cases the final product was protected against oxidative degradation by adding 400 ppm by weight NaN_3.

For concentrations higher than 5000 ppm this method of preparation was not applicable because the initial sugar/water mixture demanded a percentage of sugar which exceeded the saturation point. For this reason, we used a larger quantity of water in the initial solution. This exceeding quantity was let to evaporate while agitating continuously at a temperature of 40°C. This procedure lasted several days.

The M1 fluid is a solution of polyisobutylene in a kerosene / polybutene solvent (7/93 %w. respectively). The A1 fluid is a more concentrated solution (2% w/v) of the same polymer in dekalin. The molecular weight in the first case is $3.8 \cdot 10^6$ and in the second $4.3 \cdot 10^6$. They have both been the object of International Workshops (Combloux 1989, Villard-de-Lans 1991) and their shear and elongational properties have been extensively studied by many authors [ex. 17, 18, 29].

2.3.2. Rheometrical characterization in shear

The M1 fluid is very slightly shear-thinning. Binding et al [17] give shear flow data for temperatures varying from 20 to 70°C. They show that the variation of η_0 with temperature obeys the Arrhenius relationship:

$$\eta = \alpha\, e^{\beta/T} \qquad (2.3)$$

with $\alpha = 3.7 \cdot 10^{-9}$ Pas and $\beta = 6000°K$, and they fit the variation of η with $\dot{\gamma}$ by the Cross model:

$$\frac{\eta}{\eta_0} = \frac{1}{1+(K\dot{\gamma}\eta_0)^n} \qquad (2.4)$$

with $K = 3 \cdot 10^{-6}$ Pa^{-1} and $n = 0.385$.

Hudson and Jones [18], in an overview of the results presented with various laboratories on the fluid A1, fit the shear viscosity data with the Carreau-Yashuda model:

$$\frac{\eta-\eta_\infty}{\eta_0-\eta_\infty} = [1+(\lambda\dot{\gamma})^{2\alpha}]^{\frac{(n-1)}{2\alpha}} \qquad (2.5)$$

with $\eta_0 = 21.8$ Pas, $\eta_\infty = 0.0202$ Pas, $\alpha = 1.1$, $n = 0.34$ and $\lambda = 3.43$ s at 20°C.

The shear viscosity of the polyoxyethylene (PEO) solutions was measured with a "Carrimed Controlled Stress Rheometer" (solutions of c<4%) and a "Rheometrics RMS" controlled rate Rheometer (concentrated solutions). The 4% solution was measured with both instruments and excellent agreement was found. The normal stresses of the two most concentrated polyoxyethylene solutions (4 and 10%) were measured with the "RMS". The "Carrimed" was also used to verify the data given in the literature for the PIB fluids.

The cone-plate geometry was mainly used though some results have been verified by the coaxial cylinder geometry in the "Carrimed". The angle of the cone has been 1° for the "Carrimed" and 5.7° for the "RMS" rheometers (radius of 3 cm and 2.5 cm respectively). Fig. 2.1 shows the variation of the shear viscosity with the shear gradient for various concentrations, and the first normal difference coefficient for the two most concentrated solutions (4 and 10%). All measurements were performed at a constant temperature of 20°C.

The pure PEO polymer was tested with the "Gottfert Rheograph 2001" rheometer at 100°C. A long die was used (L= 20mm, D= 0.5mm), in order to avoid entry effects. The results were perfectly represented by the equation:

$$\eta = 3.73\ 10^5\ \dot{\gamma}^{-0.85} \qquad (2.6)$$

Fig. 2.2 shows the η_0 and n versus the concentration. The scaling of the η_0 in the concentrated range is $\eta_0 \sim c^{3.6}$ which, given the discussion in section 1.1.2.4., suggests

that the sugar/water solvent used here is a good solvent for PEO. At about the same concentration range (1% - 10%), but in aqueous solutions of PEO (Mw= $5 \cdot 10^6$), Tam and Tiu [20] find much higher values of the concentration dependence ($\eta_0 \sim c^5$). Powell and Schwarz [21] found $\eta_0 \sim c^{4.1}$ for aqueous solutions of PEO of Mw between $2.9 \cdot 10^6$ and $3.8 \cdot 10^6$.

Graessley [22] proposed a characteristic time connected to the shear properties of a solution:

$$\lambda = \frac{(\eta_0 - \eta_s)\, M}{c\, R\, T} \qquad (2.7)$$

where η_s is the viscosity of the solvent, M the molecular weight of the polymer, c the concentration in weight per volume and R the universal gas constant. The characteristic times for the various concentrations are shown at table 2.1.

By plotting the reduced shear viscosity of the solutions versus the product of this characteristic time with the shear gradient we obtain the master curve of Fig. 2.3. Four different temperatures were used in the case of the 4% solution and two for the 10% solution. The observations matched perfectly for the 4% and 10% polyox solutions and the A1 fluid. This is not the case for the lower concentration solutions (c<4% PEO and the fluid M1).

Considering the relative viscosity [23] as :

$$\frac{\eta}{\eta_s} = \eta_{rel} = 1 + [\eta_0]\, c + k' [\eta_0]^2 c^2 + \ldots \qquad (2.8)$$

the intrinsic viscosity :

$$[\eta_0] = \lim_{c \to 0} \frac{\eta_0 - \eta_s}{c.\eta_s} \qquad (2.9)$$

and the Huggins coefficient :

$$k' = \lim_{c \to 0} \frac{\eta_{rel} - [\eta_0] \,.\, c - 1}{([\eta_0]\, c)^2} \qquad (2.10)$$

for the polyoxyethylene solutions were found respectively : $[\eta]_0 = 700$ cm^3/g and $k' = 0.24$. These values are about half the ones found for aqueous solutions of the same polymer but of a Mw= $4.2 \cdot 10^6$ by James and McLaren [24] in a study of laminar flow through porous media (1500 cm^3/g and 0.4). Powell and Schwarz [21] report an

intrinsic viscosity of 1040 cm^3/g for aqueous solutions of PEO and Kalashnikov and Vlasov [25] 300 cm^3/g for Mw= $4 \cdot 10^5$.

The Mark-Houwink relationship :

$$[\eta] = K \cdot M^a \qquad (2.11)$$

has been previously determined for this polymer (PEO WSR-301) by Shin [27] and Stone and Stratta [26]. They both agree for a= 0.78 but for K they found $1.03 \cdot 10^{-2}$ and $1.25 \cdot 10^{-2}$ respectively when $[\eta]$ is expressed in cm^3/g. Our results agree with those of Stone and Stratta (Fig. 2.4).

The molecular weight of our polymer has been verified by the Gel Permeation Chromatography technique (Appendix D), since it has been in stock for about 15 years and degradation with time has been previously reported [21]. The number-averaged and weight-averaged molecular weights were found : $M_n = 5.7 \cdot 10^5$ and $M_w = 8.5 \cdot 10^5$ respectively and the polydispersity: $(M_w/M_n) = 1.48$.

The overlap concentration for the PEO solutions (eq. 1.13) is found: $c^* \cong$ 1000ppm. As can be seen in the plot of the specific viscosity versus the reduced concentration (Fig. 2.5), hydrodynamic interactions at rest do not exist for concentrations lower than or equal to this concentration. The polymer contribution to the zero shear rate viscosity is linear with concentration. Chain overlapping exists from this concentration till 1%. At higher concentrations, the power law increase of η_0 with c indicates the existence of entanglements.

Mochimaru [28] reviewing the results of many investigators, reports on the same polymer a linear relation between specific viscosity and reduced concentration for reduced concentrations inferior to 1, which is the case in our study too. For reduced concentrations higher than about 15 he finds a slope of about 6, much higher than the slope of 3.6 in our case. This fact, together with the lower Huggins coefficient value than the one reported by James and McLaren, indicate that the existence of the saccharose in our solvent reduces polymer-polymer interactions at rest and increases solvent quality.

The characteristic time of the M1 fluid used in this study agrees with the one reported in [29] and found by modeling this fluid by the three-mode Maxwell model. As shown by Nguyen and Sridhar [32], at room temperature M1 is close to θ conditions. M1 is in the transition concentration regime, whereas A1 is a semi-dilute solution.

Table 2.1. Shear viscosity and characteristic times of the PEO and PIB solutions.

polym	Mw (g/mol)	$[\eta]$ (cm^3/g)	k'	c (ppm)	T (°C)	c_U (g/lt)	η_0 (Pas)	$[\eta_0]c_U$	λ (s)
PEO	10^6	700	0.24	0	20	0	0.0235	0	0
				10	20	0.0124	0.0237	0.0087	0.0067
				50	20	0.0620	0.024	0.0434	0.0067
				100	20	0.1240	0.025	0.0868	0.0067
				500	20	0.62	0.035	0.434	0.0074
				1000	20	1.24	0.0488	0.868	0.0081
				2000	20	2.48	0.0705	1.74	0.0155
				5000	20	6.20	0.2363	4.34	0.140
				10000	20	12.4	0.680	8.68	0.217
				40000	17	49.6	214	34.7	1.76
				40000	20	49.6	178	34.7	1.47
				40000	23	49.6	156	34.7	1.29
				40000	26	49.6	148	34.7	1.22
				100000	19	124	6210	86.8	20.6
				100000	23.7	124	4600	86.8	15.2
PIB				0	20	0	1.6	0	0
(M1)	$3.8 \cdot 10^6$	290	0.50	2440	20	2.12	2.97	0.615	1.00
PIB(A1)	$4.3 \cdot 10^6$			22700	20	20	21.8		1.93

2.4. Experimental setup for the orifice flow.

Two submerged (SJC) and one free jet (FJC) configurations were used. As discussed in Chapter 1, free and submerged jet configurations give the same flow curves since the same relationship between energy losses and pressure drop exists for both of them, in large contraction ratios and for capillary forces at the free surface negligible. This theoretical result has been confirmed by experiments.

In 2.4.1 we describe the free jet configuration and a submerged one based on glass tubes, and in 2.4.2 an U-shaped submerged jet configuration.

2.4.1. Glass tube configurations.

In the case of the SJC (Fig.2.6), the orifice plate (1) was tightly held between two glass tubes (2), of internal diameter 20mm (Appendix B). The upper tube was connected to the upstream reservoir (3). The flow of the fluid (4) out of the geometry took place through a flexible tube (5), sufficiently long and thin to minimize exit instabilities. Its free end (6), could be fixed at different positions. The flow then occurred due to gravity induced pressure head between the free surface into the reservoir and the position of the free end of the tube.

The pressure drop has been measured with an inductive pressure transducer (8)(HBM, type PD1, class 1, nominal Dp= 0.1 bar), the signal of which was amplified and digitalised (9). The transducer was connected to a pair of holes (7) available on the test-geometry, symmetrically placed with respect to the orifice plate, at sections where upstream and downstream flow is steady.

The flow rate has been controlled by the help of a precision balance (PA OERLIKON AG, Precisa mod 400 M, maximum weight 404 g, d_d= 0.001 g) (10) whose electrical signal has been recorded by a SEFRAM type SRM recorder.
The temperature in the reservoir was recorded by a digital thermometer (11) (Digitec United Systems Corporation), measuring up to 0.01°C.

By removing the lower of the two tubes we obtained a free jet configuration, which allowed to examine the aspect of the extrudate as the SJC was essentially used for low flow regimes and FJC for intermediate and high flow regimes.

2.4.2. The U-shaped configuration.

The second submerged jet configuration, which allowed us to achieve very low pressure drop values, was based on a different, very simple conception. The orifice plate has been held between two glass tubes whose ends were machined to form an U-shape (Fig. 2.7). The flow took place due to level differences created between the two tubes. Given the very low flow rates involved with these experiments, the pressure drop was taken equal to the hydrostatic pressure of a fluid column of height equal to this level difference. For very low level differences, a strong influence of even slight temperature variations was observed on the total length of the fluid column, and so, the whole configuration was kept into a constant temperature bath (20 +/- 0.01°C). The level differences were measured by a cathetometer with a precision of 10μm.

2.5. The flow curves.

2.5.1. The solutions.

The fluids used in the present study were passed through orifices of diameters varying from 0.2 mm to 1.2 mm. The upstream tube diameter was in all cases 20 mm giving a very large contraction ratio (from 16.7 to 100). The influence of the orifice diameter on the flow regimes has thus been negligible as will be shown later. Inertial effects have also been negligible since Re was rarely superior to 7. This value is considered by Happel and Brenner [33] to characterize the onset of inertial effects.

It was shown previously [5] that in the case of a large contraction ratio and if capillary forces on the surface of the fluid are neglected, for both free and submerged jet configurations, the pressure drop is simply related to energy losses and no correction term is needed. In the present study, the flow curves obtained with each one of the different setups are presented together.

The extrudate in the case of the free jet exited in some cases (low viscosity solutions at low regimes) in the form of drops. No discontinuity in the flow curves has been noticed during the passage from the drop form to the jet form.

The evolution of the behavior of the flow curves with concentration is shown in Fig. 2.8. Distinct behavior has been observed in the dilute, semi-dilute unentangled and entangled solutions, as they are defined by Fig. 2.5. The behavior of the dilute solutions (PEO solutions of c<2000 ppm) is similar to the one described in section 2.2 : the sequence of the slopes 1, 2 and again 1 is found as the regime is increased, giving respectively evidence of the dominance of viscous stresses due to the solvent contribution, of elastic stresses due to unraveling of the chains and again viscous stresses due this time to additional dissipation arising from hydrodynamic interactions of the unraveled chains. During the second (elastic) regime vortex growth takes place. The Reynolds number took in general values between 0.3 and 7, though some experimental points for very low concentrations arrived till 15.

In the semi-dilute non-entangled range (5000 ppm $\geq$ c $\geq$ 2000 ppm for the PEO solutions and the M1 fluid), an additional scaling of $P_g \sim q_v^4$ occurs (Fig. 2.8 and 2.10), showing that hydrodynamic interactions occur during the unraveling of the chains, since the equivalent hydrodynamic radius necessary to release such interactions is reached for lower molecular extension than in the dilute range. The Reynolds number varied from 0.1 to 10. The subsequent break of slope observed at higher flow rates corresponds to the onset of 3D unstable flow as will be discussed in 2.6.3.

For both the dilute and the semi-dilute unentangled concentration ranges elastic phenomena dominate the flow and shear thinning is rather negligible (certainly in the dilute range). But shear thinning becomes important in the entangled range. The flow

curves of the solutions in this range follow a slope inferior to 1 at low regimes (0.7 for the 4% PEO and the A1 fluid and 0.55 for the 10% PEO). It is followed by a much steeper slope at intermediate regimes for a range of flow rates that diminishes with concentration (Fig. 2.8 and 2.9). This slope increase was observed in all orifice diameters tested (Fig. 2.9). It varies between 2 and 4. Along this regime the build up of the 3D upstream instabilities is observed in the form of intermittent knitting. A third and final regime with smaller slopes (1 for the PEO 4% and 0.3 for the PEO 10%) is observed at higher flow rates. This is the regime where knitting instabilities become permanent resulting in the melt fracture phenomenon of the extrudate, and in huge drop formation for the much more mobile A1 fluid. The Re varied from 3.10^{-4} to 5 for the experiments on this range.

In Fig. 2.9, the pressure drop P_g is plotted as a function of an effective rate of deformation, defined by [5, 11] :

$$\dot{\gamma} = 8 \frac{3n+1}{n} \frac{q_v}{\pi D^3} \qquad (2.12)$$

This representation makes data obtained with different diameters collapse on a single curve for each solution. This indicates that in the contraction ratio range used in the present study the contraction ratio effects can be absorbed in the definition of $\dot{\gamma}$.

For the concentrated solutions, as concentration is increased, the $\dot{\gamma}$ value where the slope increase takes place increases and the extent of this intermediate regime is reduced. The flow curve tends thus to the typical form of the one observed with polymer melts with a stable part followed by an unstable regime where the slope of the pressure drop - shear rate relation is lower [11, 12]. In order to verify that PEO would follow the general behavior observed there with PDMS and polybutadiene, the pure polymer was tested in a similar orifice geometry.

2.5.2. The pure polymer.

As already mentioned, the PEO polymer has been provided in the form of powder. Its melting point is 70°C. The configuration described in 2.4.1 is not convenient to test the pure PEO because of the high temperatures and pressures demanded. The "Gottfert Rheograph 2001" rheometer was thus used for this purpose. It is a controlled speed instrument with upstream reservoir diameter D= 12mm.

The die used has a diameter of 0.5mm (contraction ratio of 24) and a length of 0.2mm. The experiment took place at a temperature of 100°C. The speed of the piston has been varied between 5.10^{-4} and 0.3 mm/s and the corresponding pressure values

varied from 17 to 310 bar. For the lowest regimes examined, the stabilization of the pressure took as long as two hours.

The flow curve is shown in Fig. 2.11. A break of its slope at $\dot{\gamma}$= 200 s^{-1} is accompanied by melt fracture (Fig. 2.19 to 2.23).

2.6. Discussion.

2.6.1. The dimensionless representation of the flow curves.

A non-dimensional pressure drop parameter C can be constructed by dividing the orifice pressure drop ΔP_g to the one of an inelastic fluid of the same shear properties, flowing at the same q_v. This latter can be given by $2 L_{eq} \tau_w$, where τ_w equals to $\eta(\dot{\gamma})\dot{\gamma}$, with $\dot{\gamma}$ defined by eq. (2.12) and L_{eq} a known function of fluid rheology [30]. Thus :

$$C = \frac{\Delta P_g}{2 L_{eq} \tau_w} \qquad (2.13)$$

The parameter C accounts for shear thinning effects [11, 30] and, thus, it is particularly convenient to estimate the importance of elastic effects. In the case of an inelastic liquid :

$$C = 3\pi / 8L_{eq} = 2.03$$

The variation of C with the non-dimensional rate of deformation $\lambda\dot{\gamma}$ is given in Fig. 2.12 and 2.13. λ and $\dot{\gamma}$ are defined by eq. (2.7) and (2.12) respectively. As seen in these graphs, in the dilute and semi-dilute unentangled ranges, below a critical value $(\lambda\dot{\gamma})_c$, viscoelastic effects are negligible : C remains close to the value of 2.03 expected for an inelastic fluid. For PEO solutions $(\lambda\dot{\gamma})_c$= 50 whereas for the PIB solution (M1) $(\lambda\dot{\gamma})_c$= 500. This difference can be explained in terms of solvent quality : in a good solvent (PEO solutions) the molecule is swollen and so, lower stretching rates are needed in order to produce substantial molecular deformation, giving pronounced viscoelastic effects. Molecules in a θ or poor solvent (M1 fluid), will unravel at higher stretching rates.

In the dilute range C increases linearly with the product $(\lambda\dot{\gamma})$ till the constant value is obtained. For the 500ppm PEO solution, the limiting value of C is 16 and is attained for at $\lambda\dot{\gamma} > 400$. In the semi-dilute unentangled range it increases as $(\lambda\dot{\gamma})^3$, and arrives at values higher than 100 for the PEO 1% solution. According to the analysis presented in [5], the first scaling ($C \approx \dot{\gamma}$ implying that $P_g \approx q_v^2$) is due to elastic stresses

whereas the second one ($C \approx \dot{\gamma}^3$ implying that $P_g \approx q_v^4$) arises from hydrodynamic interaction as molecules are being stretched. Along both scalings, flow is governed by transient elongational effects. As will be discussed later on, departure from the power 3 scaling law at higher ($\lambda\dot{\gamma}$) is accompanied by 3D unstable flow. The power 3 scaling of C with ($\lambda\dot{\gamma}$) and a subsequent break of slope corresponding to initiation of 3D unstable flow is also observed for the M1 fluid (Fig. 2.13).

The C coefficient obtained also very high values for the concentrated range solutions but in a less pronounced way. For the PEO 4% and the A1 fluid C has the newtonian value of 2 at ($\lambda\dot{\gamma}$) of the order of unity and for the PEO 10% at even lower values. It increases as $(\lambda\dot{\gamma})^{0.25}$ for the PEO 4% and the A1 and as $(\lambda\dot{\gamma})^{0.15}$ for the PEO 10%. The decrease in slope as concentration is increased , shows a more progressive development of tensile stresses as the flow strength increases, indicating that molecular extension is less pronounced. A mechanism that can limit molecular flow induced extension can be provided by entanglements whose number increases with concentration. The subsequent slope increase observed for the 4 and 10% PEO solutions and the A1 fluid indicates that beyond a certain value of $\dot{\gamma}$, the flow stretching action becomes strong enough to overcome the entanglement effect and so, to stretch the molecules in the same manner as in dilute solutions. A fact supporting this conclusion is that as concentration is increased, higher values of ($\lambda\dot{\gamma}$) are observed for the change of slope to a higher value : as molecular entanglements increase, stronger flow conditions are required to provoke important molecular stretching.

The behavior of concentrated solutions in orifice flow can thus be summarized as follows :

At very low regimes flow is Newtonian (cf. the A1 fluid). As flow strength increases, a regime is reached where molecular extension is governed by the balance of flow induced stretching and resistance to stretching arising from entanglements. We will subsequently refer to this regime as the entanglement governed extension regime. The slope of the P_g - $\dot{\gamma}$ relation decreases with concentration and takes values from 1 to about 0.5. Transition from the Newtonian to this regime may be characterized by decreasing values of the C coefficient and subsequent increase, as suggested by the data on the A1 fluid. However, further experiments are needed to characterize the limits of this transition.

As the flow rate is further increased, flow strength is sufficient to overcome effects due to entanglements. In this molecular extension regime, molecular stretching should be essentially governed by single chain properties and should vary considerably with flow rate. The scaling along this regime is also concentration dependent and may vary from 4 to about 2 as concentration is increased. The onset of this regime, which should be considered as the extension to concentrated solutions of the intermediate

regime observed for dilute and semi-dilute unentangled solutions, is delayed in terms of ($\lambda\dot{\gamma}$) as concentration is increased. At concentrations close to the melt, where the entanglement density is very important, this regime is not observed : flow is never strong enough to produce substantial molecular extension.

2.6.2. The extensional viscosity curve.

The variation of the Trouton ratio as a function of non-dimensional rate of deformation λII_D is plotted in Fig 2.14. Tr is here defined by:

$$Tr = \left(\frac{\eta_E}{3\,\eta}\right)_{\dot{\gamma}=\sqrt{3}\dot{\varepsilon}=II_D} \qquad (2.14)$$

$II_D = (2\ trD^2)^{1/2}$ is the second invariant of the rate of deformation tensor and λ is given from equation (2.7). The master curve of shear viscosity η obtained for entangled solutions is also shown in figure 2.14. The Tr curves for semi-dilute solutions are obtained by applying the analysis of Binding (appendix C) in the entanglement governed extension regime.

For dilute solutions, this analysis may be applied in the large $\dot{\gamma}$ regime, since at lower $\dot{\gamma}$ transitional elongational effects, not accounted for, govern the flow. When P_g is linear in $\dot{\gamma}$, for constant viscosity fluids, the analysis predicts a constant η_E value for the 500ppm PEO solution (solid line in figure 2.14).

The $\eta_E(\dot{\varepsilon})$ curve is also predicted to reach a second plateau value $\eta_{E\infty}$ by the model of Cartalos and Piau [5]. This curve is characterized by an abrupt transition from $3\eta_0$ to $\eta_{E\infty}$ when $\dot{\varepsilon}\cong 1/\lambda$ (dashed line for the 500ppm PEO solution in Fig. 2.14). $\eta_{E\infty}$ represents dissipation due to hydrodynamic interaction and increases linearly with polymer concentration.

As shown in Fig. 2.14, semi-dilute solutions show a different elongational behavior. The evolution of $\eta_E(\dot{\varepsilon})$ is more progressive for a given concentration, indicating that entanglements limit molecular extension. Also, elongational properties become less important (lower Tr values) as concentration, and so the degree of entanglements, is increased.

2.6.3. Flow instabilities.

The pattern of the flow upstream was visualized for most of the solutions reported in the present study by the technique described in appendix B. Pictures of the flow were also taken.

2.6.3.1. The dilute range.

In the dilute range, an initial Newtonian flow regime took place at very low flow rates. It was followed by the vortex growth regime. Observation follow the same lines as the ones reported in [4, 7]. No large scale 3D instabilities were observed for concentrations lower or equal to 500ppm of PEO.

2.6.3.2. The semi-dilute unentangled range.

In this range of the PEO solutions (2000 ppm to 1%) lip vortices existed at the lowest regimes examined. They grew until they occupied the whole upstream diameter. The vortex growth regime for the 1% solution lasted until the pressure of 250 mbar. In higher regimes and as the size of the vortices remained constant, a small scale instability of a frequency of several Hz occurred : The fluid particles in the main flow region followed paths of an "S"-form. As the regime was increased slowly, this instability occupied the whole region near the orifice including the vortices (Fig. 2.15). Above P_g= 1 bar, a large scale 3D instability occurred. The flow happened in the following way : A small volume of the fluid from some distance upstream "rushes" out of the orifice and then flow stops for a small time interval till the same phenomenon is repeated again for another fluid "pack" emerging from a different point of the upstream region ("knitting" flow). The amplitude of this instability as well as the vortex size increased with flow rate for the regimes examined (until P_g= 10 bar).

For the 5000 ppm PEO solution the vortex growth regime existed until P_g= 400 mbar. At higher regimes the above mentioned S-form instability was observed. At initial stages after the onset, when the instability occupied only a very small region near the orifice, it was characterized by partial oscillatory motion along the particle trajectory (secondary motion consisting of a back and forth motion along the trajectory). At higher pressures, lateral oscillation (S-form) characterized the secondary motion. For regimes higher than 900 mbar "knitting" flow was observed.

In a general manner, the instability build-up in this concentration range follows the sequence:

i) small back and forth oscillations along the trajectory in the main flow region (discontinuous acceleration), ii) S-form flow lines and iii) knitting. (ii) and (iii) develop gradually : the region of the S-form flow lines grows as back and forth oscillations disappear (Fig. 2.16). At a higher regime, knitting occurs, which, in its intermittent stage coexists with S-form flow lines (Fig. 2.17). In Fig. 2.17 intermittent knitting exists and in Fig. 2.17b it becomes permanent.

The small scale instabilities reported here are of the same type as the ones reported by Cartalos and Piau [4]. The evolution from back-forth oscillation to S-shaped instabilities seems also coherent with the one reported in [9, 10]. The important point is that the onset of these small scale instabilities occurs along the intermediate regime. Their existence does not affect the scalings predicted by the similarity analysis in [5, 6]. It is thus concluded that these instabilities give small perturbations to a mean velocity and stress field and they do not affect considerably molecular extension.

However, departures from the $P_g \approx \dot{\gamma}^4$ or equivalently the $C \approx (\lambda\dot{\gamma})^3$ scalings, predicted by the theory in [5, 6], occurs at the same time as the upstream flow is governed by large 3D instabilities (knitting flow).

2.6.3.3. The entangled range.

The concentrated PEO solutions are not completely transparent, a fact that diminished the visualization possibilities upstream. However, intermittent knitting was observed in the intermediate regime, as mentioned at section 2.5. It became gradually permanent with the increase of the flow rate. In the final regime of both PEO 4% and 10% (slopes 1 and 0.3 mentioned at section 5), melt fracture of the extrudate (Fig. 2.18) accompanied the upstream knitting with the same frequency.

A similar behavior was observed for the A1 fluid as far as the regimes lower than the knitting regime are concerned. During the knitting regime the flow had a periodic pattern : huge drops were formed at the exit of the orifice plate while the knitting frequency was moderate. In the following the drop fell, pulled by its own weight, and the knitting frequency increased by about an order of magnitude. This pattern lasted for some seconds and the drop formation started again. The whole cycle lasted about 30 seconds.

Table 2.2. The flow parameter values in the onset of the instabilities.

solution	d (mm)	q_v (10^{-3}ml/s)	Pg (mbar)	$\dot{\gamma}$ (10^{-3} s^{-1})	$\lambda\dot{\gamma}$	C	type
PEO 0.5%	0.2	13.4	282	17.8	249	16.2	S
0.5%	0.2	18.2	944	24.2	339	41.8	knitting
1%	0.26	22.5	310	13.6	295	22.6	S
1%	0.53	165	315	12.4	268	24.7	S
1%	0.26	31.5	900	19.4	425	55.2	knitting
1%	0.53	264	860	19.8	430	47.8	knitting
4%	0.53	36.0	951	3.39	6000	25.0	inter. knit.
4%	1.2	441	706	3.57	6320	18.2	inter. knit.
4%	0.53	93.0	4340	8.75	15400	77.9	knitting
10%	0.26	4.12	3000	3.75	56900	22.7	inter. knit.
10%	0.53	36.6	3000	4.11	62500	22.2	inter. knit.
10%	0.26	10.1	10000	9.17	139300	59.1	knitting
10%	0.53	76.2	8000	8.56	130200	48.2	knitting
M1	0.53	17.8	606	1.21	1210	19.7	knitting
A1	0.26	4.32	97.8	3.29	6350	21.7	knitting

2.6.3.4. The pure polymer.

At the lowest regimes examined, the sharkskin phenomenon existed (Fig. 2.19). At higher regimes the sharkskin disappeared and small scratches covered the surface of the extrudate (Fig. 2.20 and 2.22). At regimes on and higher than the rupture of the slope (unstable flow), melt-fracture occurred (Fig. 2.21 and 2.23).

2.6.4. Further dimensionless representation.

Since the upstream flow is governed by extensional effects, a non-dimensional number measuring the importance of extensional stresses is needed. One possible candidate is the stress ratio S_{el}, defined by :

$$S_{el} = \left(\frac{\tau_{zz} - \tau_{rr}}{\tau_{rz}}\right)_{orifice} = \left(\frac{\eta_E(\dot{\varepsilon})\,\dot{\varepsilon}}{\eta(\dot{\gamma})\,\dot{\gamma}}\right)_{\dot{\varepsilon}=\dot{\varepsilon}_{max},\ \dot{\gamma}=\dot{\gamma}_{max}} \qquad (2.15)$$

$\dot{\varepsilon}_{max}$ and $\dot{\gamma}_{max}$ are the maximal elongational and shear rates on the orifice plane. All quantities in eq. (2.15) can be related to experimental measurements through the analysis of Binding (Appendix C).

The pressure drop ratio C is plotted as a function of S_{el} in Fig. 2.24 for the concentrated solutions and the PEO melt. It is shown that data at stable flow conditions collapse on a single curve. Moreover, the onset of unstable flow occurs when S_{el} exceeds a value close to 12.

2.7. Conclusion.

This study was concerned with the evolution of the flow behavior in the orifice geometry of polymer solutions as the concentration is varied from the dilute to the entangled range. The different concentration ranges were defined by examining the different regions of the variation of the zero shear rate viscosity as a function of reduced concentration.

The flow through an orifice of PEO solutions as well as of two standard polyisobutylene solutions (M1 and A1 fluids) was examined. The flow curves were determined and flow kinematics and stability were investigated in an extended range of flow parameters.

Several conclusions arise from this study :

2.7.1. Flow curves.

The flow curves of dilute and semi-dilute solutions confirm and extend previous results on molecular interpretation.

For dilute and semi-dilute unentangled solutions, departure from Newtonian behavior occurs at a value of $(\lambda\dot{\gamma})$ of about 50. The subsequent intermediate regime is characterized by pronounced flow induced molecular unraveling. For dilute solutions, elastic stresses are dominant which gives the $P_g \approx q_v^2$ relation. For semi-dilute unentangled solutions, hydrodynamic interaction between molecules as they are being stretched prevails. The corresponding scaling is $P_g \approx q_v^4$. For the highest flow rates, where molecules are fully stretched, flow is governed by hydrodynamic interaction. The corresponding theoretical scaling is $P_g \approx q_v$. This final scaling was observed for dilute solutions. For the semi-dilute unentangled solutions, large scale instabilities were initiated in the upstream flow before this final regime could be reached.

For semi-dilute entangled solutions, departure from Newtonian behavior is also followed by a power law relation between P_g and q_v. The flow rate exponent is much lower than the 2 or 4 exponent observed at lower concentrations, and decreased with concentration. It is argued that, in this regime flow induced molecular extension is limited by molecular entanglements. This regime is termed as the entanglement governed extension regime. At higher flow rates, a further regime is reached where P_g increases as a power of q_v from 2 to 4. It is considered that at the onset of this regime, flow strength is sufficient to overcome the effect of entanglements, so that very important molecular extensions occur. This regime is the extension to more concentrated solutions of the intermediate regime observed for low concentration solutions. The onset of this regime occurs for higher values of $\dot{\gamma}$ as concentration is increased and its extent is reduced.

At very high concentrations, close to the melt conditions this regime is not observed: it seems that entanglement effects limit molecular extension even at the highest flow rates.

2.7.2. Elongational properties.

In the dilute and semi-dilute ranges the elongational viscosity presents an abrupt transition : it increases towards a second plateau at a critical stretch rate. Trouton ratios reach very high values. In the concentrated range entanglements limit molecular extension, and the Trouton ratio increases more slowly and takes lower values as concentration is increased.

No evidence of decreasing Trouton ratio is found.

2.7.3. Dimensionless representation

The representation of the flow curves in the form $P_g(\dot{\gamma})$ accounts for the effect of the contraction ratio.

The coefficient C (the ratio of the pressure drop to the one expected for an inelastic fluid) presented an abrupt transition for every concentration in the dilute and intermediate concentration ranges. The onset of this transition was delayed in the case of a θ solvent in terms of $(\lambda\dot{\gamma})$. A dimensionless number S_{el} accounting for elongational effects was constructed. S_{el} is the ratio of elongational to shear stress on the orifice plane. The C - S_{el} representation makes data from different concentration in the semi-dilute entangled range collapse on a single curve.

2.7.4. Flow stability.

Two kinds of instability were observed: a small scale instability and a large scale 3D instability : knitting flow. In agreement with other investigations [5, 9, 10] , the former are initiated at very early stages subsequent to the appearance of the viscoelastic lip vortex, at the beginning of the intermediate flow regime. Back and forth motion of fluid particles along the streamlines in the upstream converging flow close to the orifice plane is their initial form. As flow strength is increased oscillations perpendicular to the streamlines are generated that give S-shaped flow lines. These small scale instabilities seem to give negligible perturbations to the velocity and stress fields since the upstream flow keeps an average 2D axisymmetric structure and the flow curves show the theoretically expected scalings. Onset and development of these instabilities should be related to the details of molecular unraveling in the actual flow field. However, at this stage the exact mechanism that generates and governs their evolution is not clear at present.

3D unstable flow, previously described as knitting flow characterizes the highest flow regimes for semi-dilute unentangled and entangled solutions as well as the melt flow. Onset of 3D unstable flow gives a break of slope, beyond which the P_g - q_v relation has a smaller slope. Occurrence of upstream unstable 3D flow gives a highly perturbed extrudate. The result of [11] that melt fracture is the transport of upstream generated instabilities is thus confirmed and extended to solutions.

It seems that 3D unstable flow is a more intensive form of the small scale instabilities generated at lower flow regimes. The dimensionless representation $\overline{C}$ - S_{el} shows that 3D unstable flow occurs for S_{el} values between 12 and 18 for concentrations varying from 4% to the pure polymer for PEO and for the A1 fluid. This suggests that 3D unstable flow is generated when elongationnal stresses dominate by an order of magnitude the shear stresses in the converging flow.

References

1. D. V. Boger, "Viscoelastic flows through contractions", Ann. Rev. Fluid Mech., 19 (1987) 157-182.
2. S.A. White, A.D. Gotsis and D.G. Baird, "Review of the entry flow problem: Experimental and numerical", J. Non Newt. Fluid Mech., 24 (1987) 121-160.
3. M. Moan, G. Chauveteau and S. Ghoniem, "Entrance effect in capillary flow of dilute and semi-dilute polymer solutions", J. Non Newt. Fluid Mech., 5 (1979) 463.
4. U. Cartalos and J.M. Piau, "Creeping flow regimes of low concentration polymer solutions in thick solvents through an orifice die", J. Non Newt. Fluid Mech., 45 (1992) 231-285.
5. U. Cartalos and J.M. Piau, "Pressure drop scaling laws and structural stress contributions for complex flows of flexible polymer solutions in thick solvents", J. Non Newt. Fluid Mech., 44 (1992) 55-83.
6. U. Cartalos and J.M. Piau, "Elastic and dissipative stress-producing mechanisms in contraction flows of polymer solutions as a function of flow strength and concentration", XI Int. Congress of Rheology, Brussels, 1992.
7. P.J. Cable and D.V. Boger, "A comprehensive experimental investigation of tubular entry flow of viscoelastic fluids.", AIChJ:
   "Part I: Vortex characteristics in stable flow", 24 (1978) 869;
   "Part II: The velocity field in stable flow", 24 (1978) 992;
   "Part III: Unstable flow", 25 (1979) 152.
8. H. Nguyen and D.V. Boger, J. Non Newt. Fluid Mech., 5 (1979) 353.
9. J.V. Lawler, S.J. Muller, R.A. Brown and R.C. Armstrong, "Laser Doppler velocimetry measurements of velocity fields and transitions in viscoelastic fluids", J. Non Newt. Fluid Mech., 20 (1986) 51-92.
10. G. H. McKinley, W. P. Raiford, R. A. Brown and R.C. Armstrong, "Nonlinear dynamics of viscoelastic flow in axisymmetric abrupt contractions", J. Fluid Mech., 223 (1991) 411-456.
11. J.M. Piau, N. El Kissi and B. Tremblay, "Low Reynolds number flow visualization of linear and branched silicones upstream of orifice dies", J. Non Newt. Fluid Mech., 30 (1988) 197-232.
12. J.M. Piau, N. El Kissi and B. Tremblay, "Influence of upstream instabilities and wall slip on melt-fracture and sharkskin phenomena during silicone extrusion through orifice dies", J. Non Newt. Fluid Mech., 34 (1990) 145-180.
13. G. Chauveteau, M. Moan and A. Magueur, "Thickening behaviour of dilute polymer solutions in non-inertial elongational flows", J. Non Newt. Fluid Mech., 16 (1984) 315-327.

14. K.P. Jackson, K. Walters and R. W. Williams, "A rheometrical study of Boger fluids", J. Non Newt. Fluid Mech., 14 (1984) 173-188.
15. J. Ferguson, K. Walters and C. Wolff, "Shear and extensional flow of polyacrylamide solutions", Rheologica Acta, 29 (1990) 571-579.
16. D.M. Binding and K. Walters, "On the use of flow through a contraction in estimating the extensional viscosity of mobile polymer solutions", J. Non Newt. Fluid Mech., 30 (1988) 233-250.
17. D. M. Binding, D.M. Jones and K. Walters, "The shear and extensional flow properties of M1", J. Non Newt. Fluid Mech., 35 (1990) 121-135.
18. N.E. Hudson and T.E.R. Jones, "The A1 project - an overview", J. Non Newt. Fluid Mech., 46 (1993) 69-88.
19. J.F. Joanny and S.J. Candau, Comprehensive Polymer Science, "Hydrodynamic properties", Vol. II, The syntheses, Characterization, Reaction and Application of Polymers, Sir Geoffrey Allen Ed., Pergamon Press, 1989.
20. K.C. Tam and C. Tiu, "Improved correlation for shear-dependent viscosity of polyelectrolyte solutions", J. Non Newt. Fluid Mech., 46 (1993) 275-288.
21. R.L. Powell and W.H. Schwarz, "Rheological properties of polyethylene oxide solutions", Rheologica Acta, 14 (1975) 729-740.
22. W. W. Graessley, "The entangled concept in polymer rheology", Adv. Polym. Sci., 16 (1974) 1-179.
23. R.B. Bird, R.C. Armstrong and O. Hassager, "Dynamics of Polymeric Liquids", Vol. 1, J. Wiley & Sons, 2nd ed., 1987.
24. D.F. James and D.R. McLaren, "The laminar flow of dilute polymer solutions through porous media", J. of Fluid Mechanics, 70 (1975) 733-752.
25. V.N. Kalashnikov and S.A. Vlasov, "On scale-dependent effect in laminar flow of dilute polymer solution in tubes", Rheologica Acta, 17 (1978) 296-302.
26. F.W. Stone and J.J. Stratta, Enc. of Pol. Sci. and Tech., 6 (1967) 103.
27. H. Shin, Sc.D. thesis, Massachusetts Inst. of Tech., 1965.
28. Y. Mochimaru, "Possibility of a master plot for material functions of high-polymer solutions", J. Non Newt. Fluid Mech., 13 (1983) 365-384.
29. M.S. Chai and Y.L. Yeow, "Modeling of fluid M1 using multiple-relaxation-time constitutive equations", J. Non Newt. Fluid Mech., 35 (1990) 459-470.
30. M.E. Kim, R. A. Brown and R.C. Armstrong, "The roles of inertia and shear-thinning in flow of an inelastic fluid through an axisymmetric sudden contraction", J. Non Newt. Fluid Mech., 13 (1983) 341-363.
31. R.G. Larson, "Instabilities in viscoelastic flows", Rheologica Acta, 31 (1992) 213-263 .
32. D.A. Nguyen and T. Sridhar, "Preparation and some properties of M1 and its constituents", J. Non Newt. Fluid Mech., 35 (1990) 93-104.

33. J. Happel and H. Brenner, "Low Reynolds Number Hydrodynamics", Prentice Hall ed., Engelwood Cliffs, NJ, 1965.

TABLES AND FIGURES

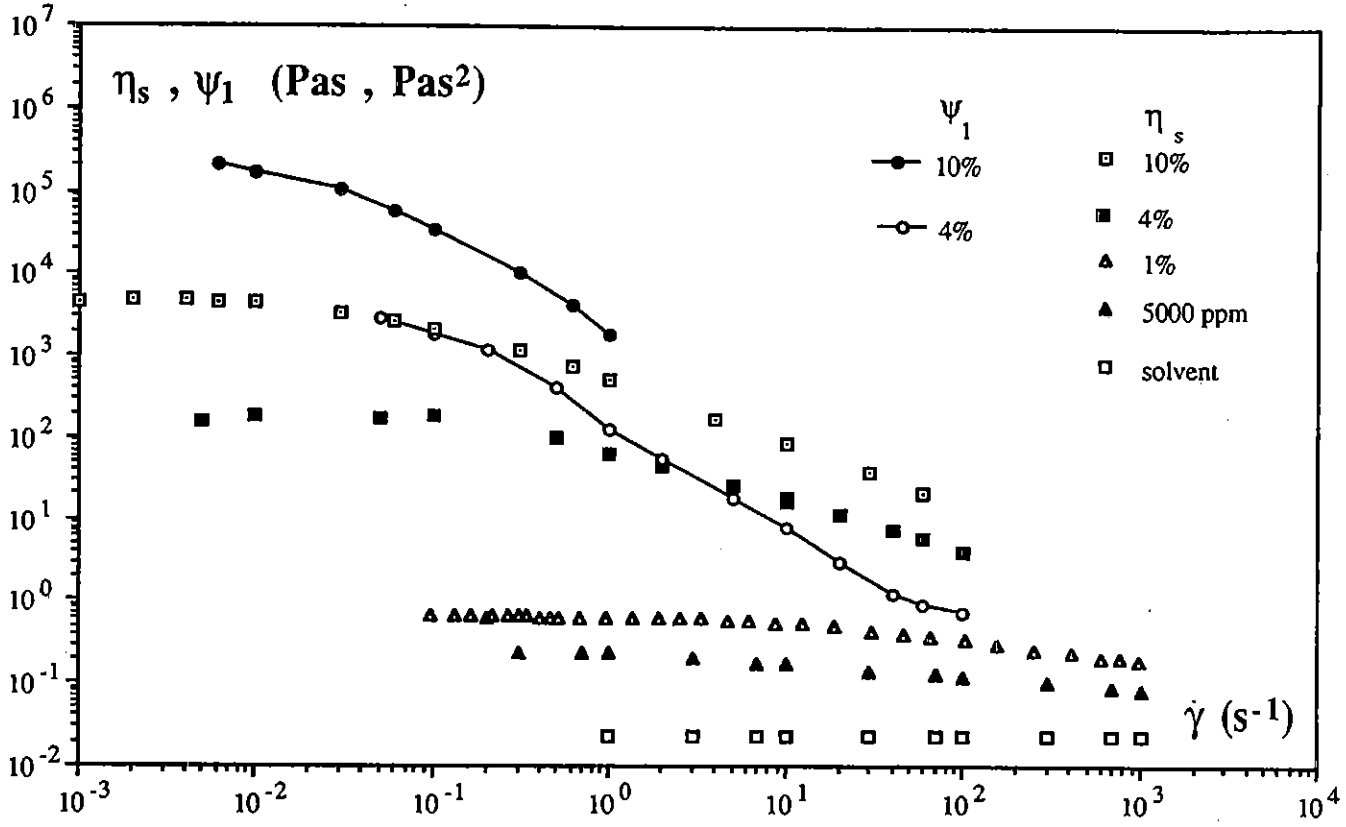

Figure 2.1 : Shear viscosity and first normal difference coefficient for the PEO solutions

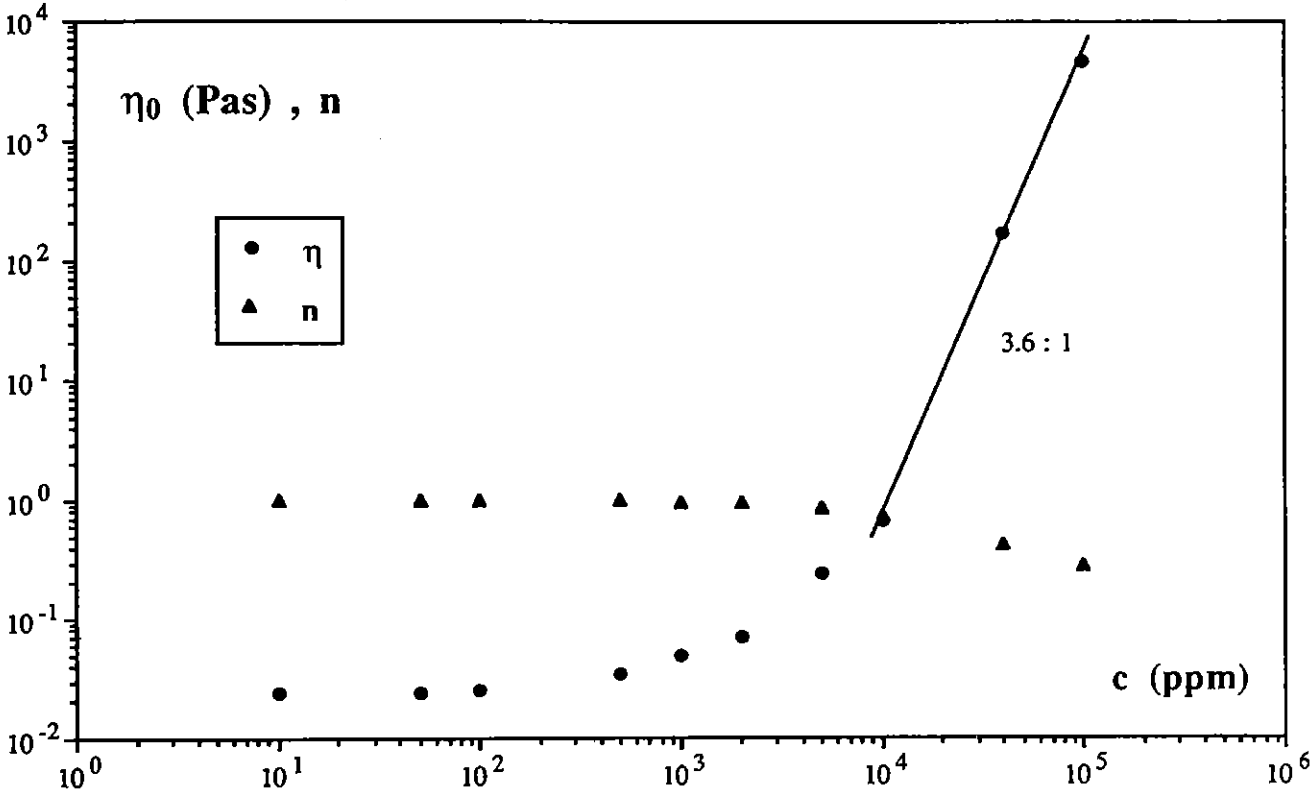

Figure 2.2 : Zero shear viscosity and power law index versus concentration for the PEO solutions

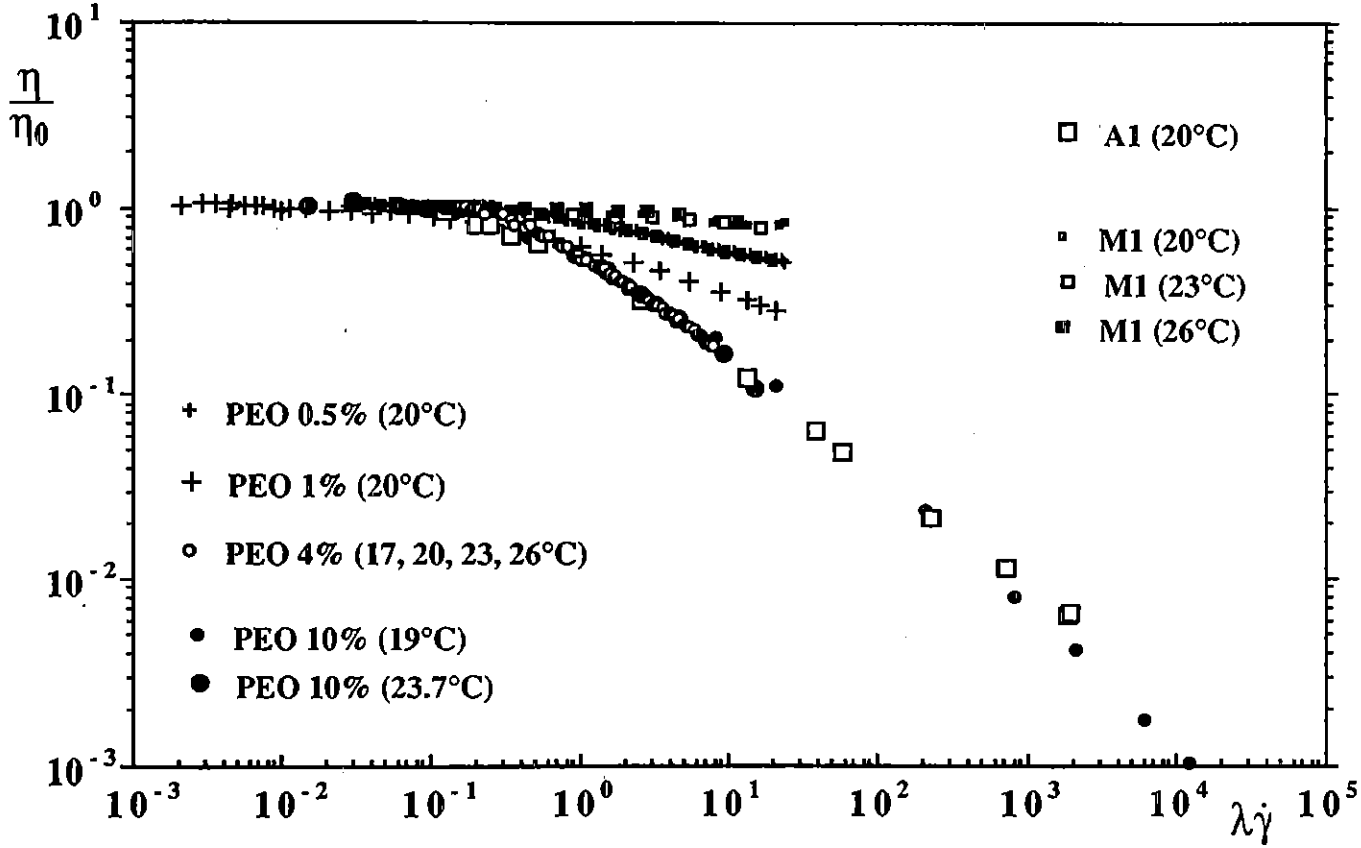

Figure 2.3 : Reduced shear viscosity versus dimensionless shear rate.

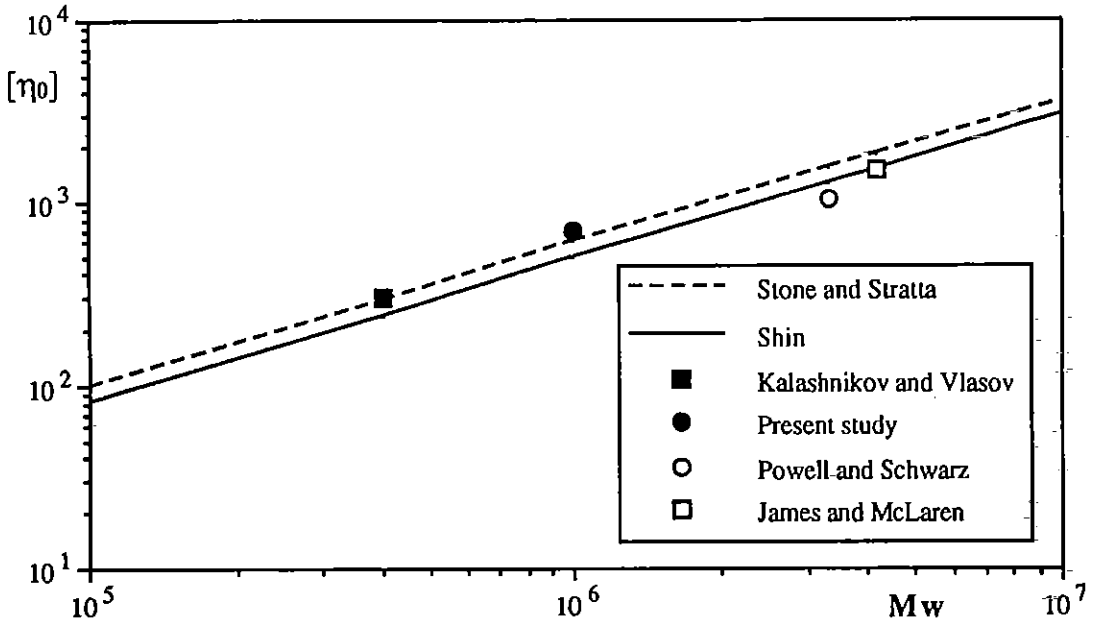

Figure 2.4 : The Mark-Houwing relationship for the PEO from various investigators.

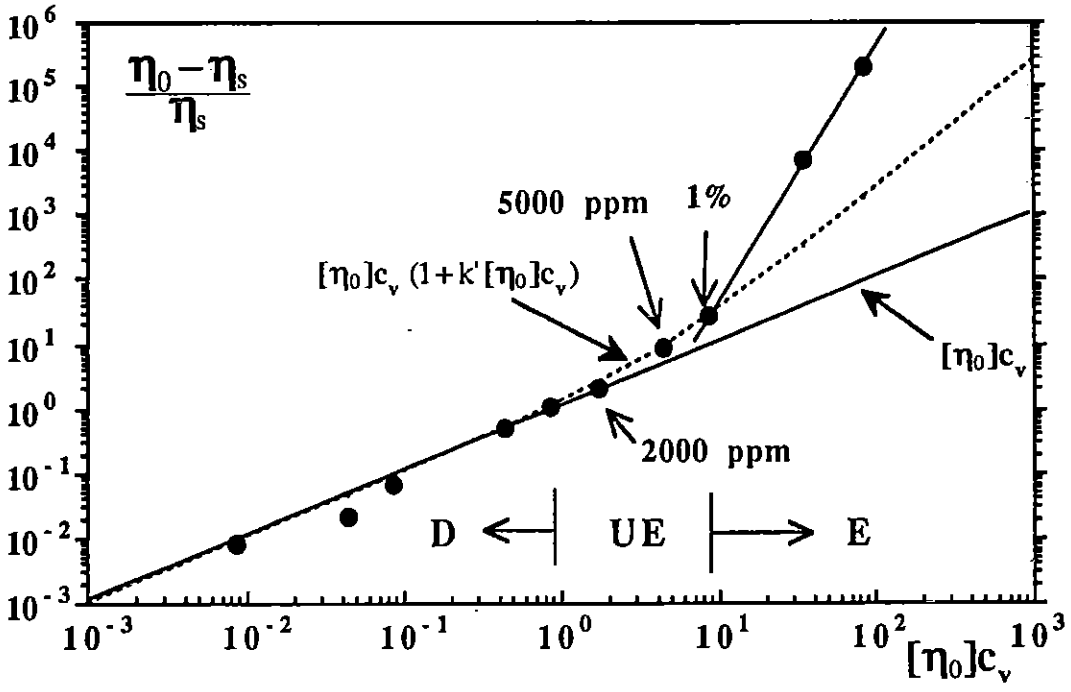

Figure 2.5 : Specific viscosity versus reduced concentration for the PEO solutions.
Distinction of the concentration regimes:
D: dilute - UE: semi-dilute unentangled - E: entangled

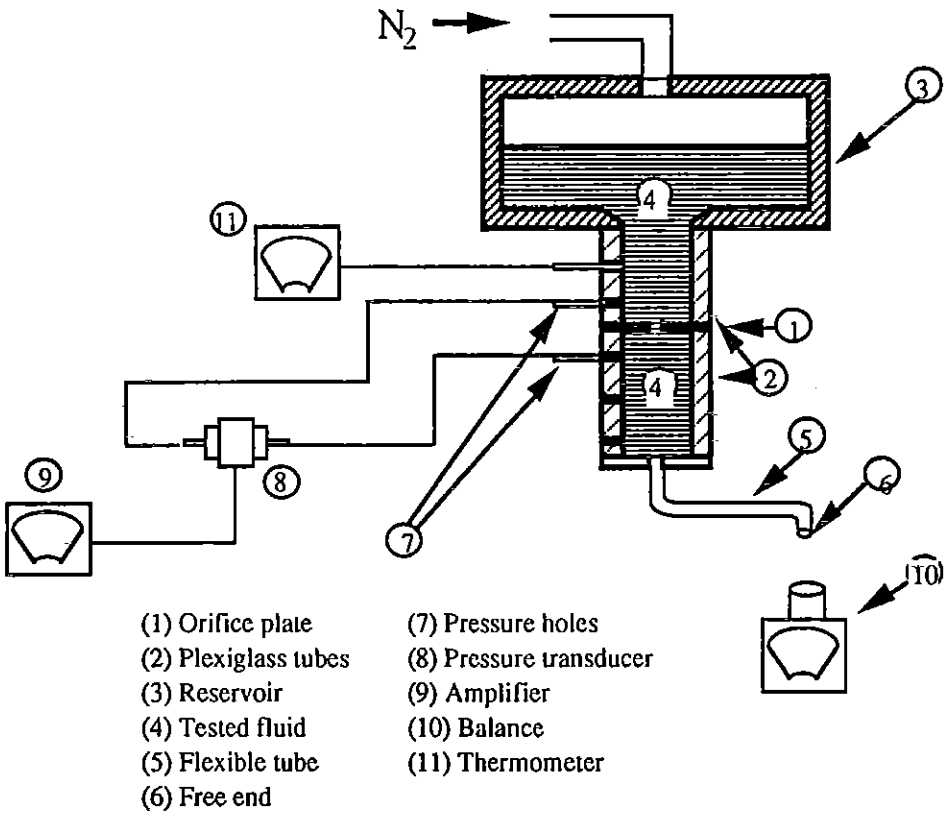

Figure 2.6 : The submerged jet configuration.

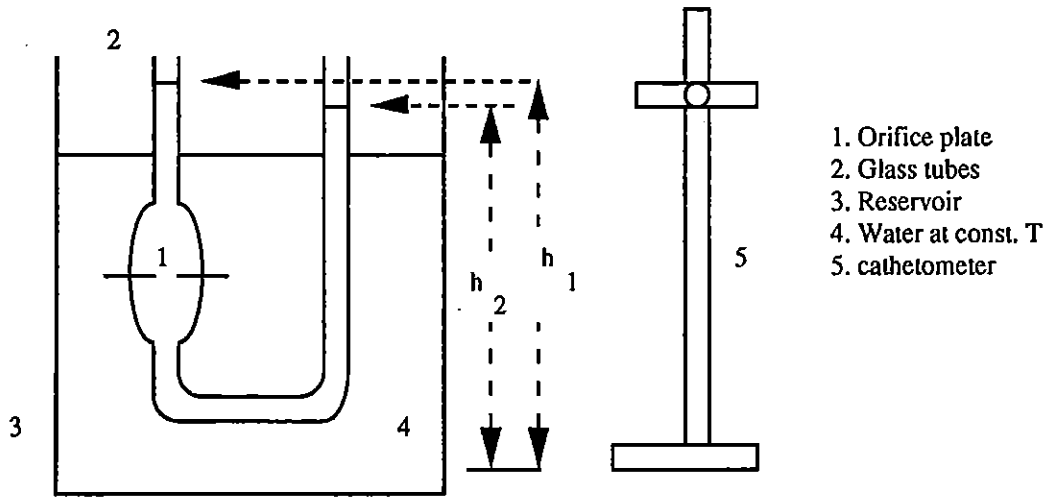

Figure 2.7 : The U-shaped submerged jet configuration for low regimes.

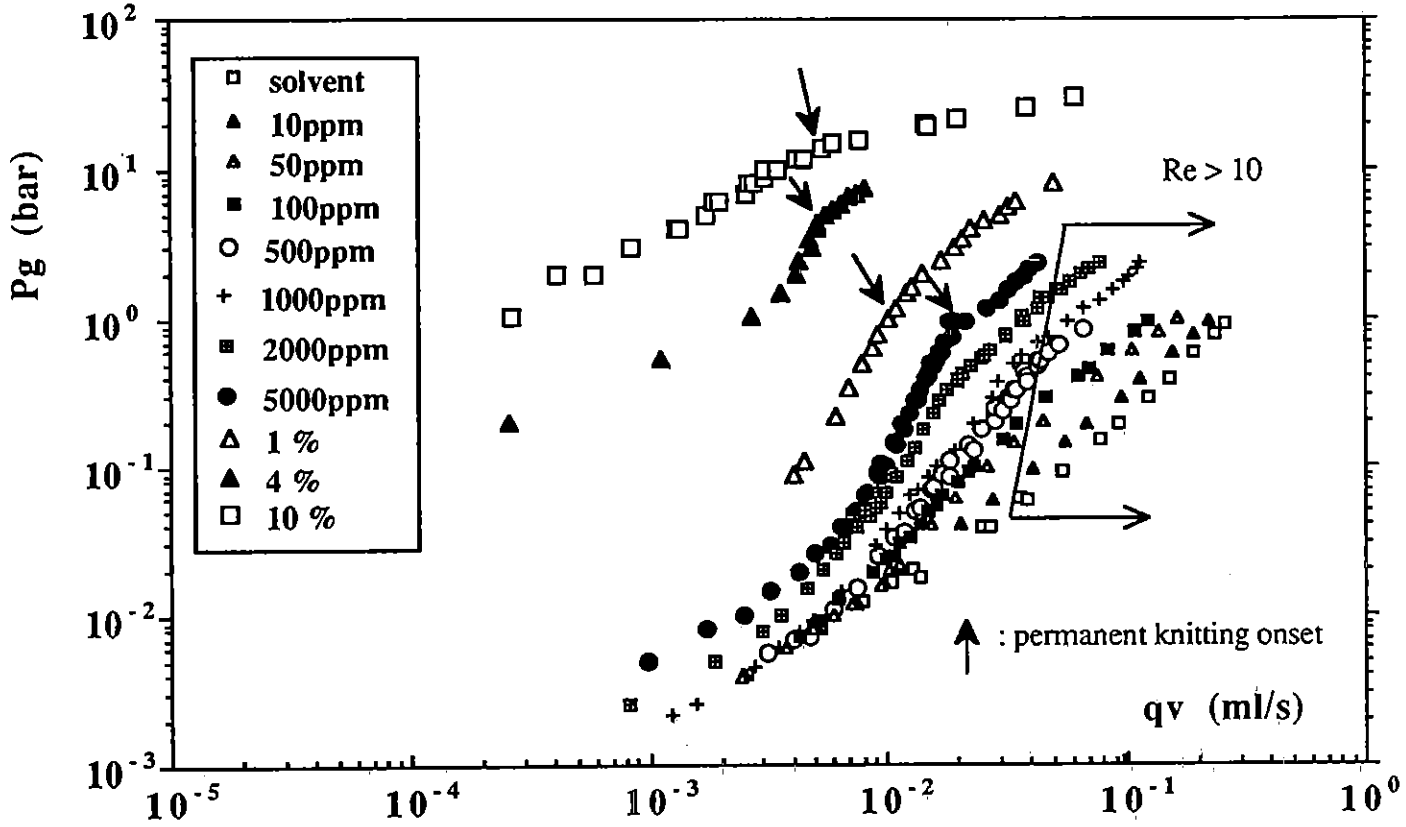

Figure 2.8 : Flow curves of the PEO solutions through an orifice of d=0.2mm.

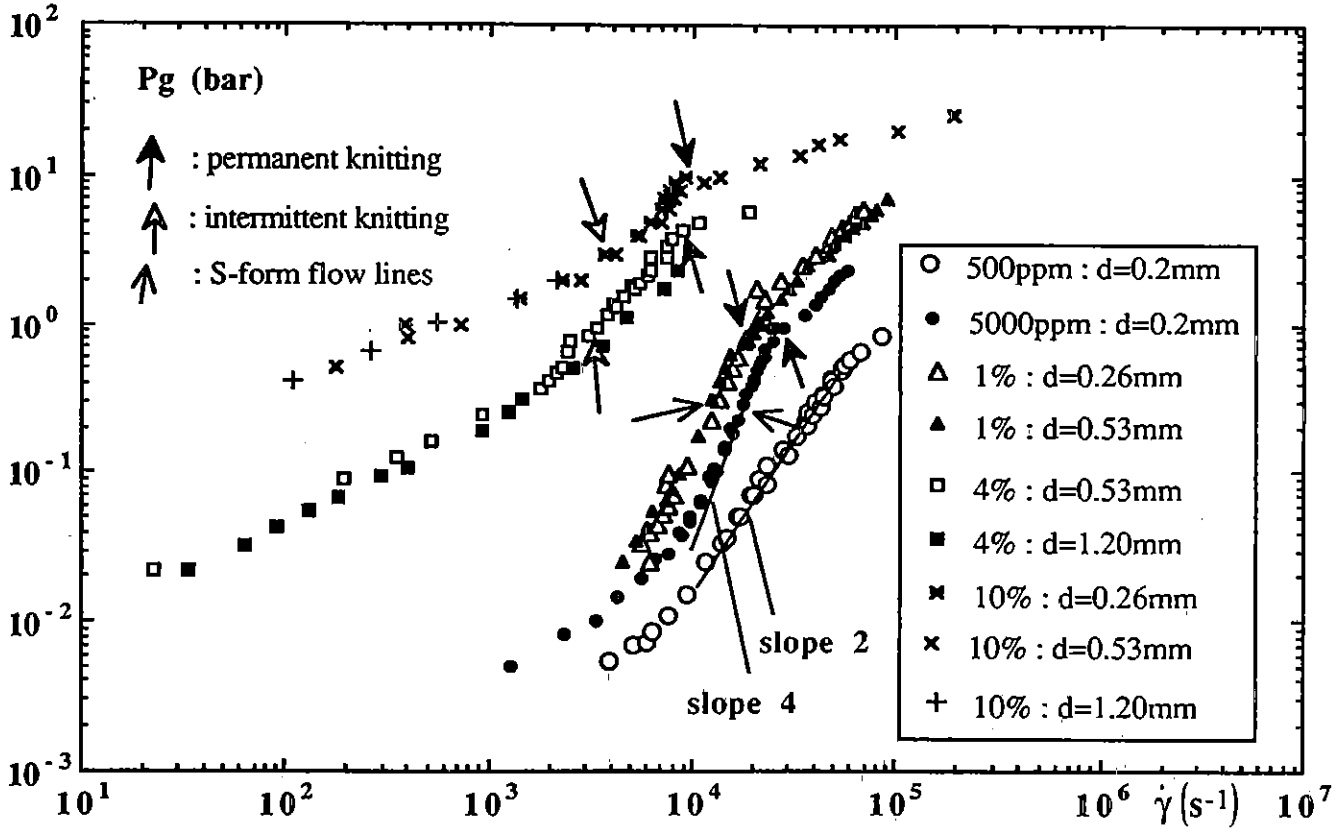

Figure 2.9 : Flow curves of the PEO solutions. The different diameter curves collapse.

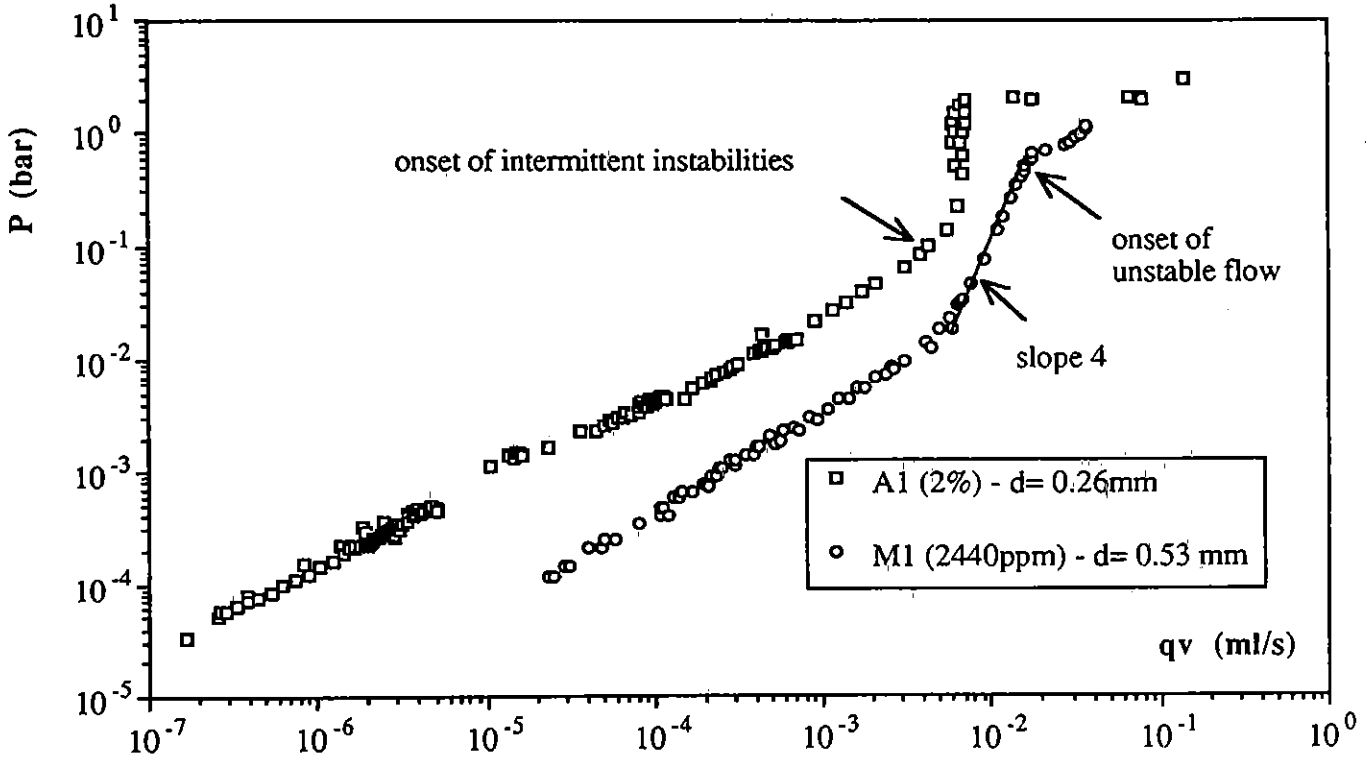

Figure 2.10 : Flow curves of the PIB solutions (A1 and M1).

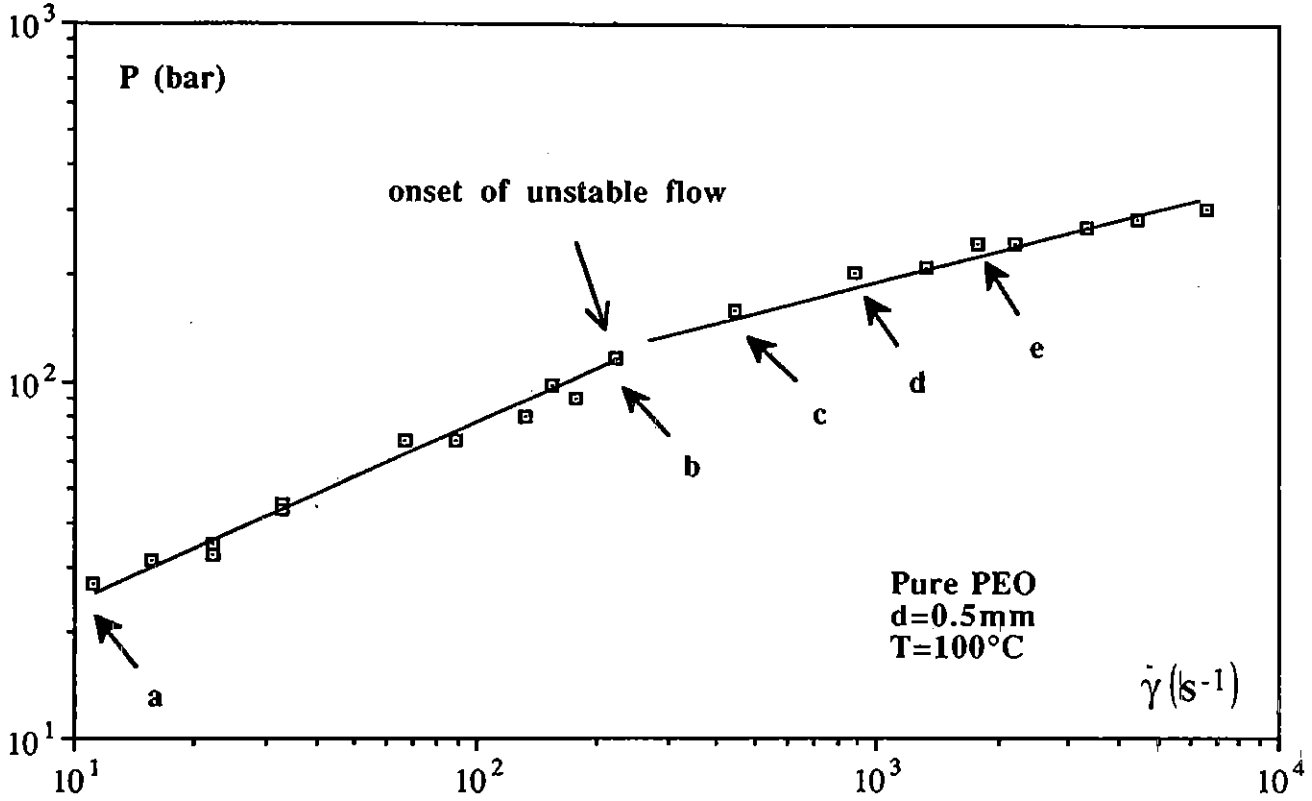

Figure 2.11 : Flow curve of the pure PEO through an orifice of d=0.5mm.
Points (a) to (e) correspond to the pictures in Fig. 2.19 to 2.23.

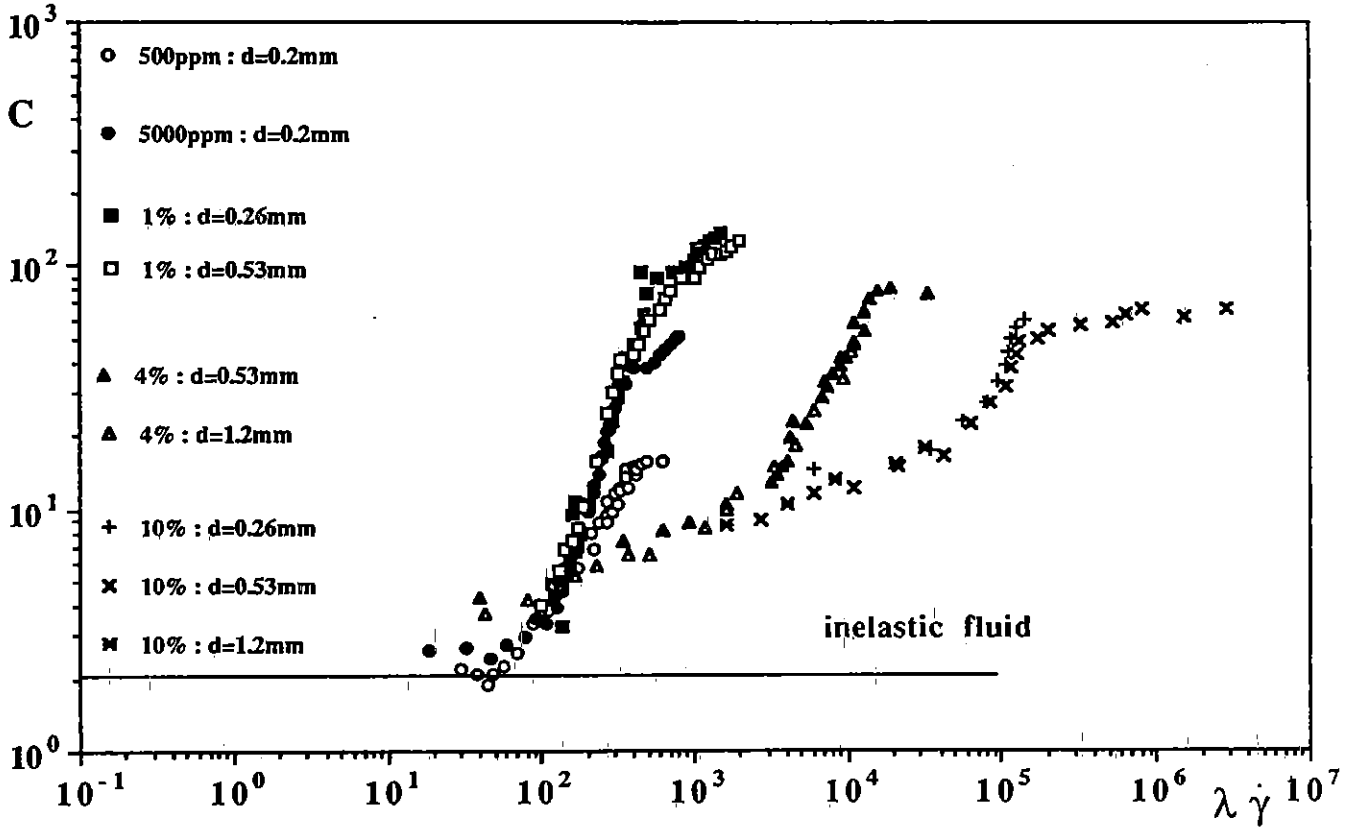

Figure 2.12 : C coefficient versus Weissenberg number for the PEO solutions.

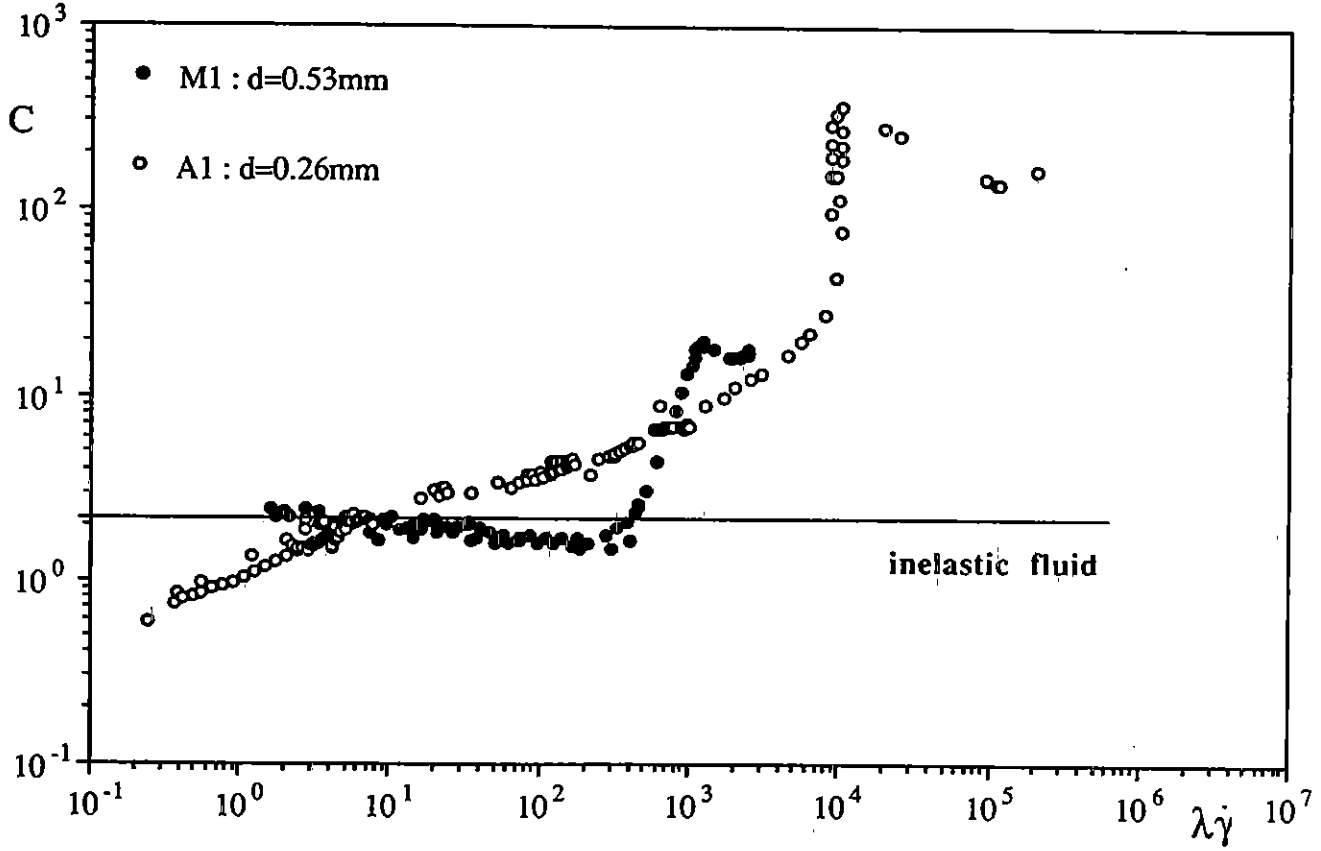

Figure 10 : C coefficient versus Weissenberg number for the PIB solutions.

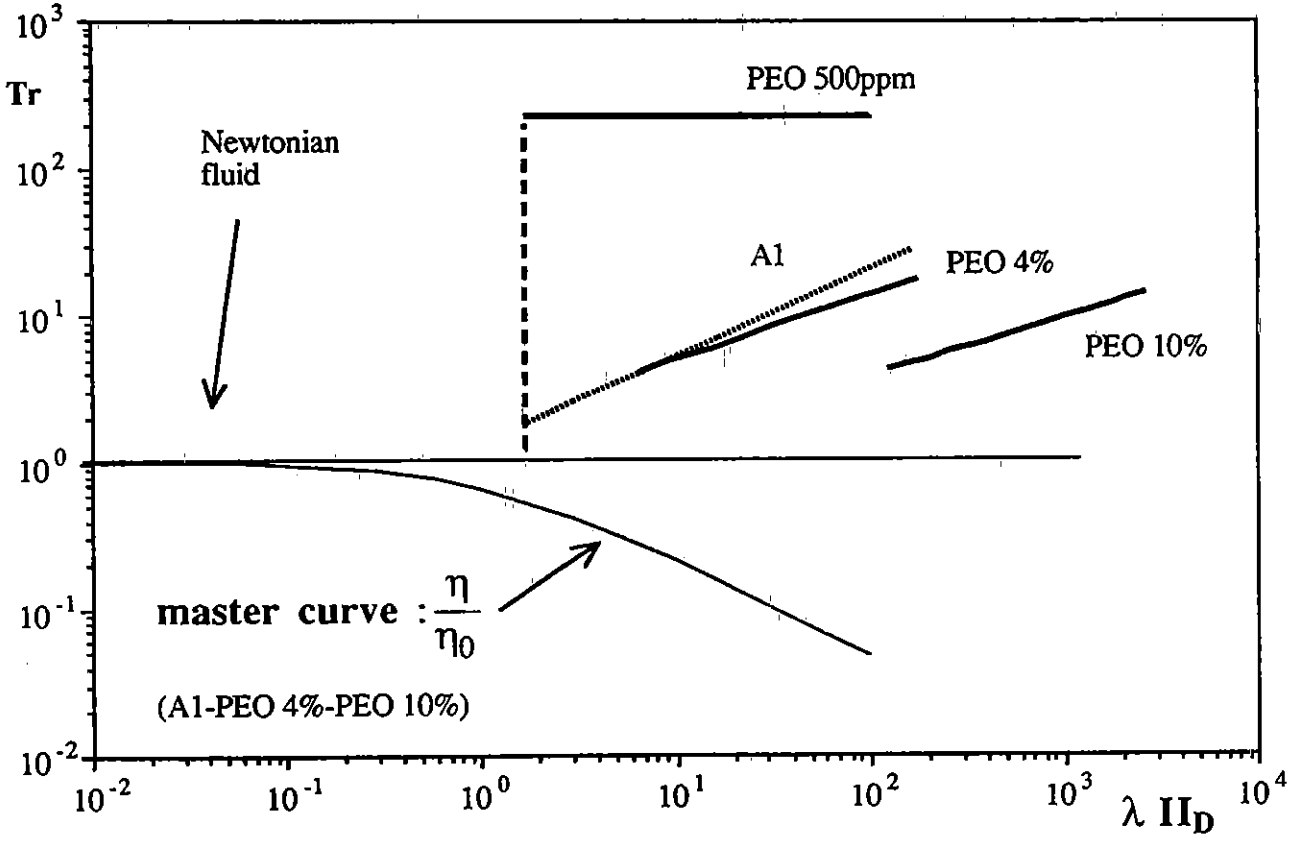

Figure 2.14 : Trouton ratio versus non-dimensional rate of deformation.

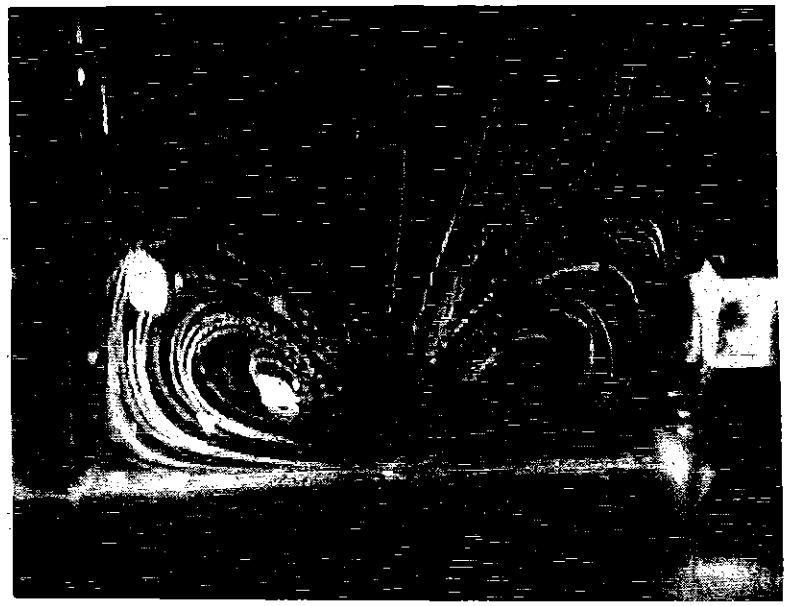

Figure 2.15 : The S-shape instability of the flow lines. PEO 1%. d=0.53mm. q_v= 0.26 ml/s, P_g= 1 bar, Re= 11, We= 643.

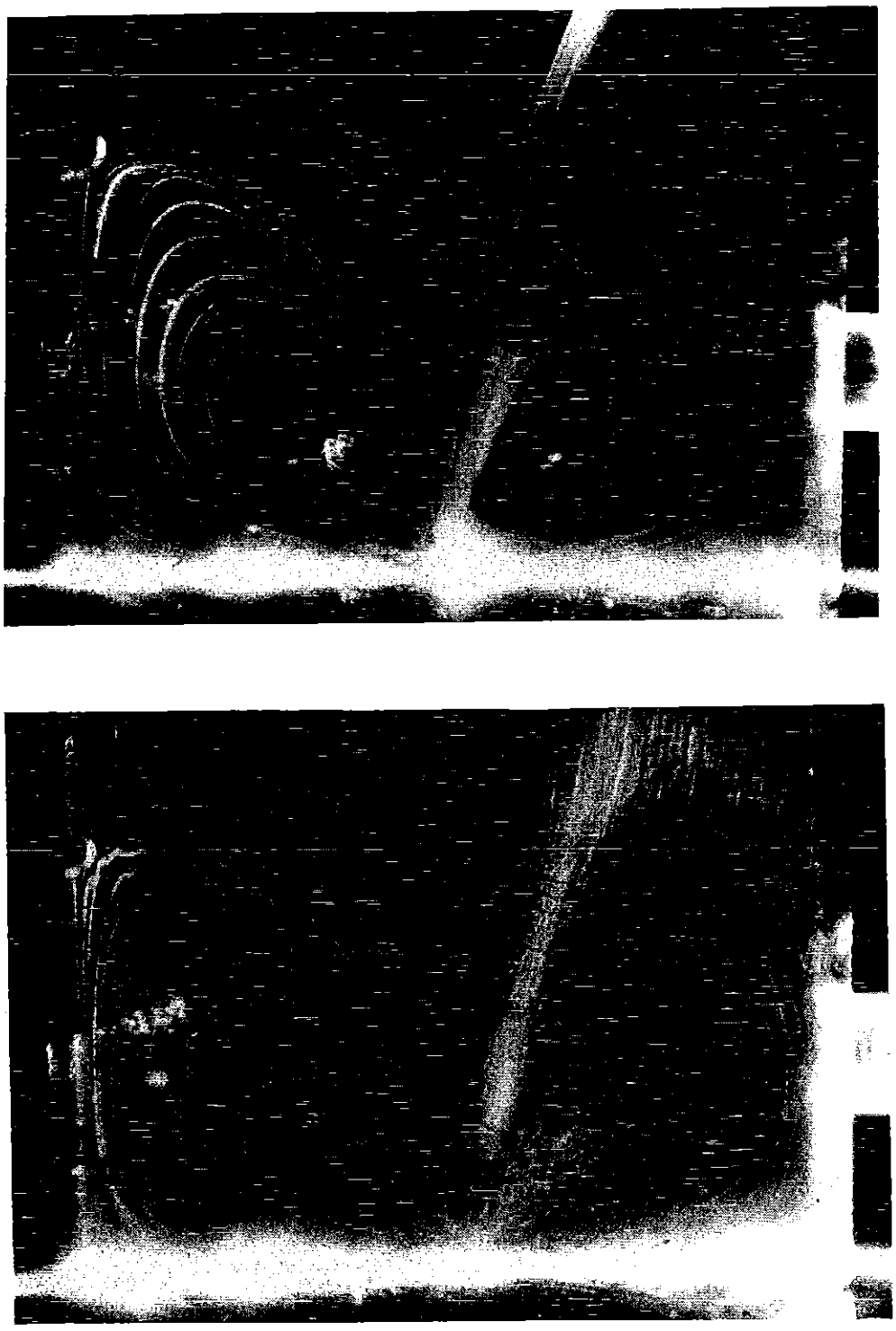

Figure 2.16 : The growth of the region of the S-form instability. PEO 1%. d= 0.53mm.
a) Pg= 0.4 bar, qv= 175 10^{-3} ml/s, $\dot{\gamma}$= 11.9 10^{3} s^{-1}.
b) Pg= 1.0 bar, qv= 285 10^{-3} ml/s, $\dot{\gamma}$= 19.4 10^{3} s^{-1}.

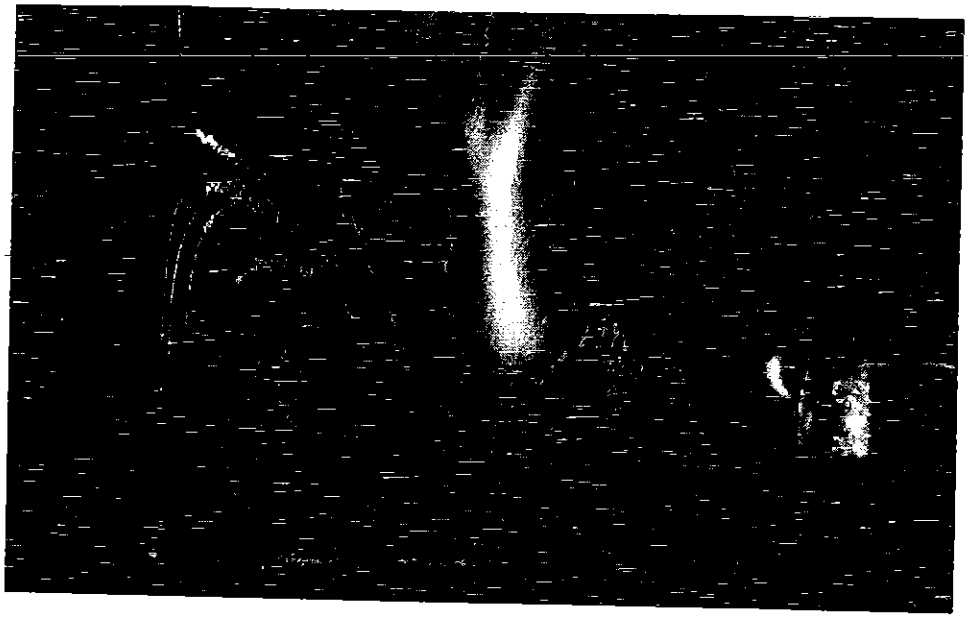

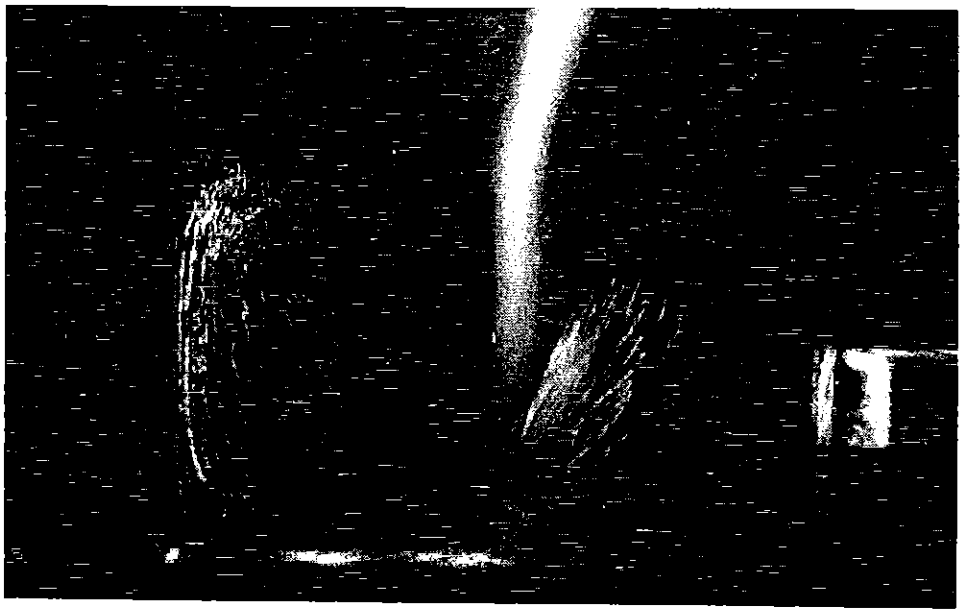

Figure 2.17 : The passage from S-type to knitting. PEO 2%. d= 0.53mm.
a) Pg= 0.5 bar, qv= 77.4 10^{-3} ml/s, $\dot{\gamma}$= 5.3 10^{3} s^{-1}, Re= 1.57, T= 0.5 min.
b) Pg= 2.0 bar, qv= 159 10^{-3} ml/s, $\dot{\gamma}$= 10.9 10^{3} s^{-1}, Re= 4.58, T= 1.0 min.

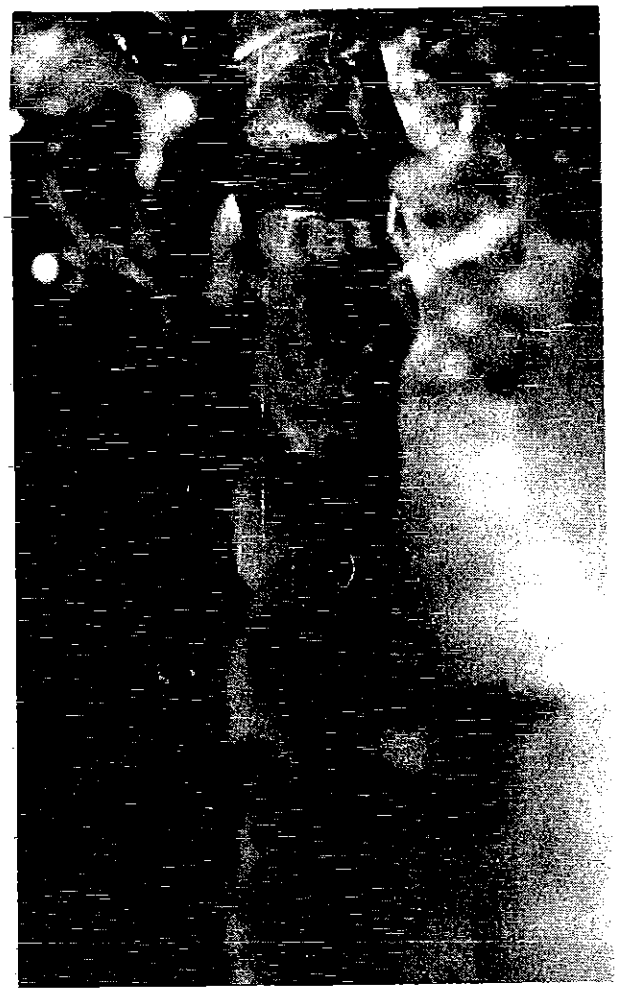

Figure 2.18 : The melt fracture in the concentrated range. PEO 10% solution. d= 0.2mm
a) Pg= 16 bar, $\dot{\gamma}$= 38580 s^{-1}.
b) Pg= 20 bar, $\dot{\gamma}$= 98500 s^{-1}.

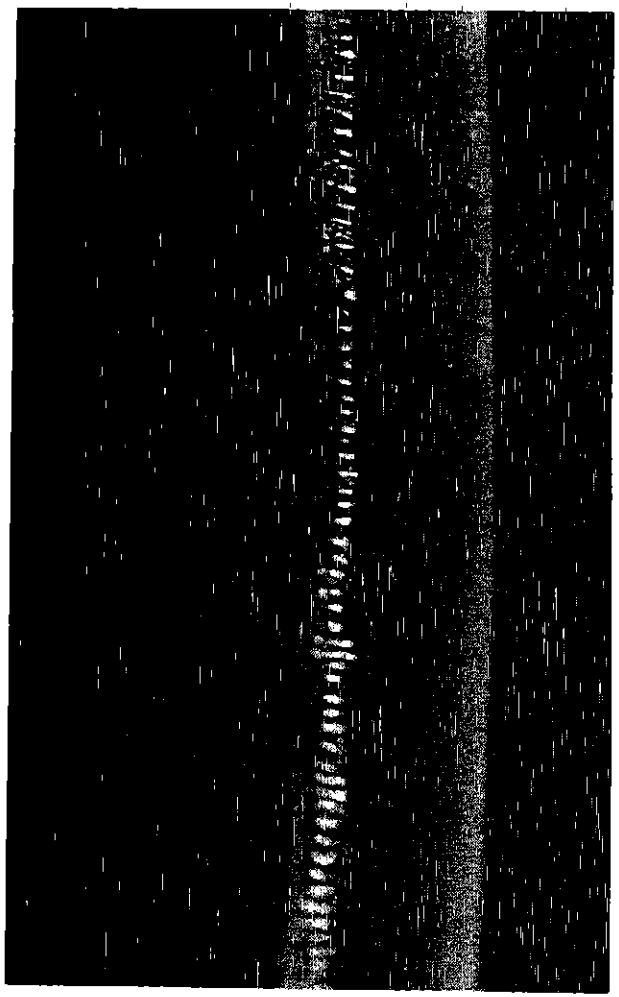

Figure 2.19 : The extrudate of the PEO powder. d= 0.5 mm. T=100°C. V_p= 5.10-4 mm/s, P= 27 bar, V= 0.29 mm/s, $\dot{\gamma}$= 11.1 s^{-1}, Re= $3.0 \cdot 10^{-9}$.

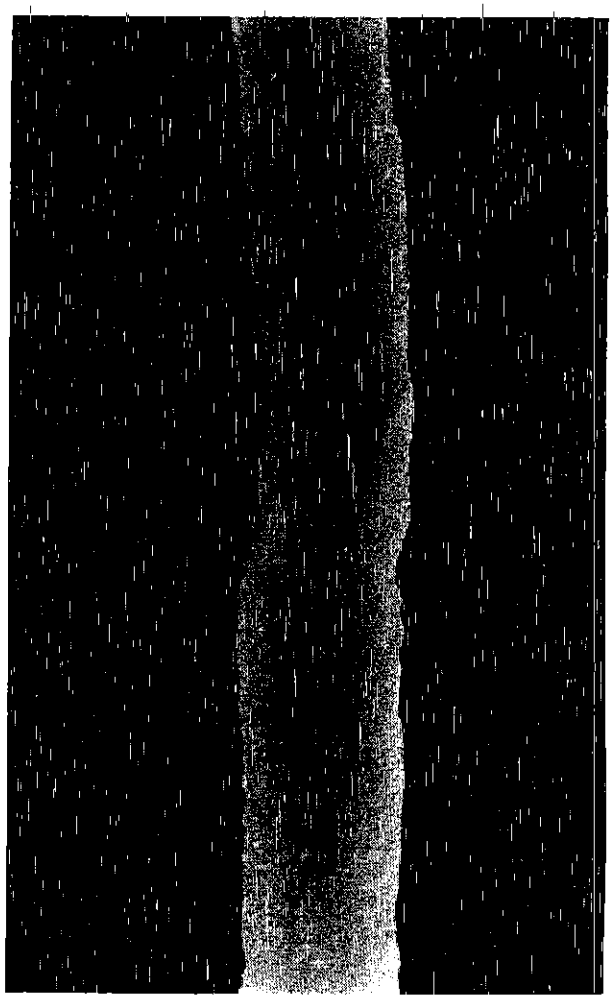

Figure 2.20 : The extrudate of the PEO powder. d= 0.5 mm. T=100°C. V_p= 10^{-2} mm/s, P= 117.5 bar, V= 5.76 mm/s, $\dot{\gamma}$= 221 s^{-1}, Re= $7.6 \cdot 10^{-7}$

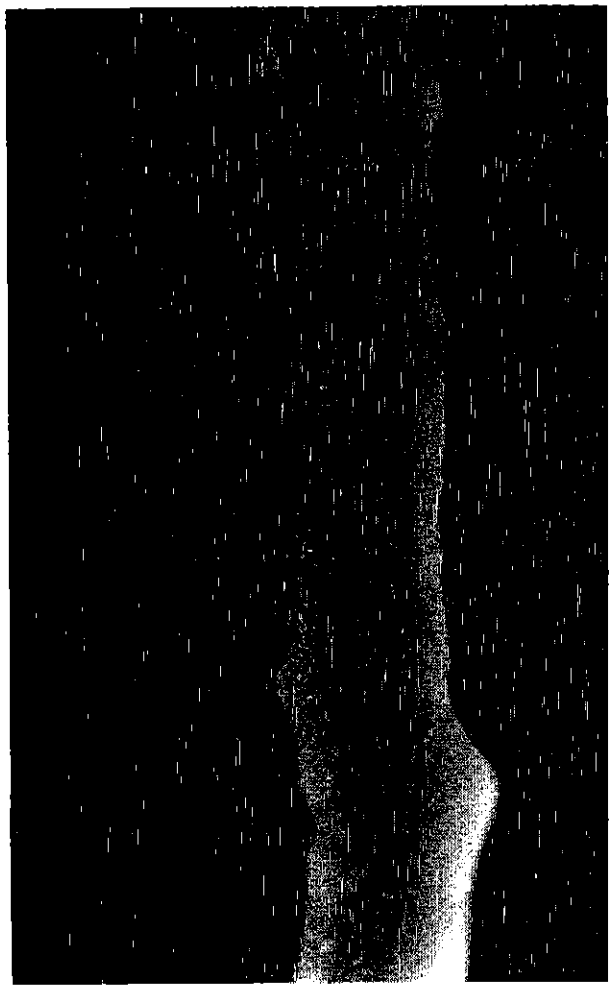

Figure 2.21 : The extrudate of the PEO powder. d= 0.5 mm. T=100°C.
V_p= 2·10^{-2} mm/s, P= 159 bar, V= 11.5 mm/s, $\dot{\gamma}$= 442s^{-1}, Re= 2.7·10^{-6}

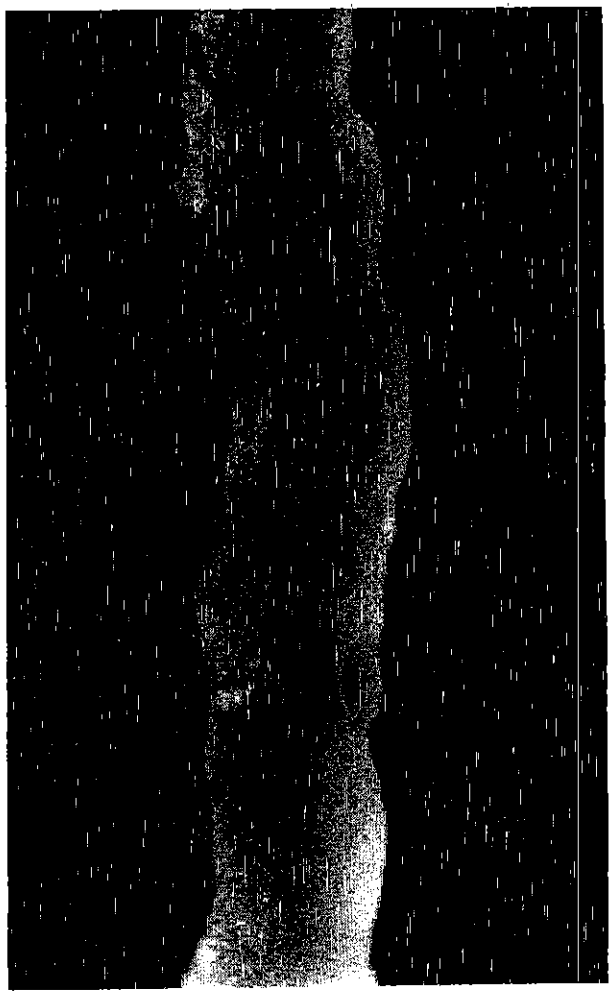

Figure 2.22 : The extrudate of the PEO powder. d= 0.5 mm. T=100°C.
V_p= 4.10^{-2} mm/s, P= 204 bar, V= 23.0 mm/s, $\dot{\gamma}$= 884s^{-1}, Re= 9.9·10^{-6}

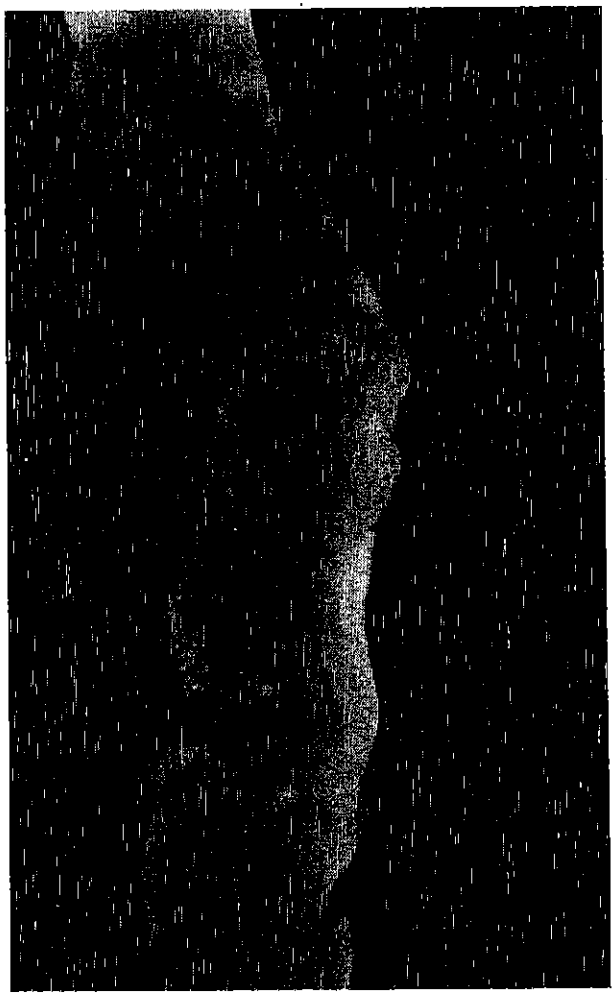

Figure 2.23 : The melt fracture phenomenon. d= 0.5 mm. T= 100°C.
$V_p = 8.10^{-2}$ mm/s, P= 244 bar, V= 46.1 mm/s, $\dot{\gamma} = 1769\ s^{-1}$, $Re = 3.6 \cdot 10^{-5}$.

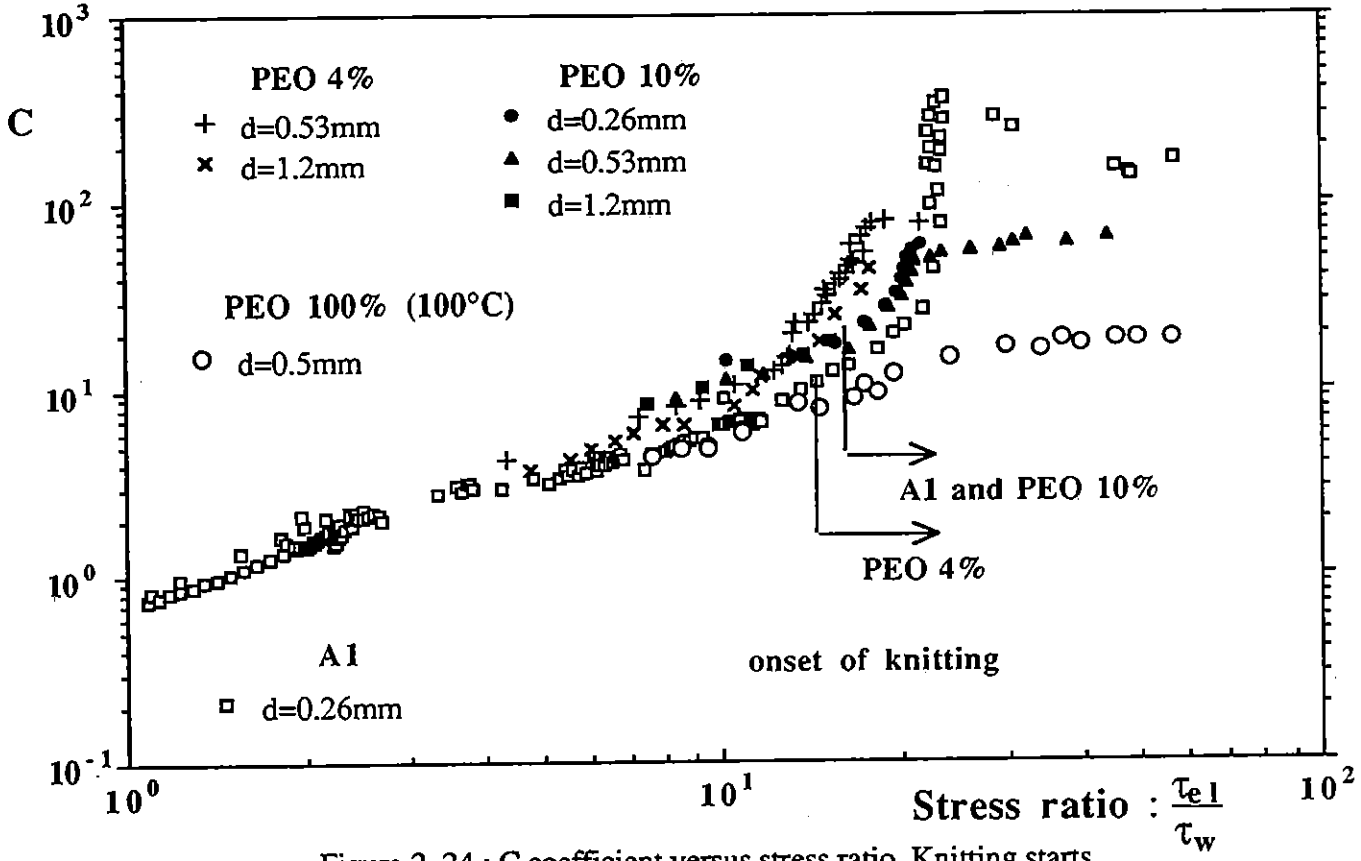

Figure 2. 24 : C coefficient versus stress ratio. Knitting starts when this ratio attains a value of about 15.

Table 2.4 : The flow curves of the PEO solutions (500 to 2000ppm).

2000 ppm (21.3°C)				1000 ppm (22°C)		500 ppm (19.5°C)	
$q_v\left(\frac{mm^3}{s}\right)$	P_g(mbar)	$q_v\left(\frac{mm^3}{s}\right)$	P_g(mbar)	$q_v\left(\frac{mm^3}{s}\right)$	P_g(mbar)	$q_v\left(\frac{mm^3}{s}\right)$	P_g(mbar)
0,82	2,6	26,80	617,1	1,23	2,2	3,11	5,5
1,89	5,1	31,10	756,1	1,55	2,5	4,06	6,8
2,94	7,7	31,30	772,0	2,72	4,5	4,71	7,2
3,52	9,9	31,43	774,0	2,74	4,7	5,01	8,5
4,63	14,8	37,01	960,0	3,47	6,1	5,93	10,9
5,41	20,1	37,30	966,0	4,30	8,0	7,41	15,3
6,10	26,1	37,30	976,0	4,82	9,2	9,12	24,6
6,50	29,9	36,90	1024,1	6,37	14,4	10,80	32,9
7,50	39,4	42,79	1164,0	8,97	28,8	13,10	49,7
7,25	39,7	47,55	1369,0	9,91	37,9	15,20	70,3
8,50	46,2	43,70	1374,0	11,22	47,3	16,90	88,1
8,09	49,9	53,16	1559,0	12,61	62,5	18,38	109,0
8,95	51,1	50,90	1564,0	13,37	68,3	21,90	141,0
9,30	55,5	58,74	1754,0	14,90	85,8	25,19	177,0
9,18	65,5	64,67	1977,0	14,98	84,1	28,27	218,0
10,00	67,3	70,13	2168,0	16,31	98,9	28,49	247,0
10,90	84,3	68,90	2174,0	19,50	127,0	31,90	295,0
10,50	89,7	77,89	2374,0	23,00	194,0	33,99	333,0
12,10	108,8			27,90	291,0	37,30	432,0
13,20	133,1			29,42	378,0	42,40	510,0
14,20	176,1			34,00	492,0	52,20	655,0
15,80	226,1			37,07	558,0	66,70	850,0
16,50	277,1			42,90	690,0	11,77	36,1
17,80	324,1			46,71	763,0	13,72	51,2
19,60	379,1			55,90	947,0	15,81	71,5
19,60	382,1			56,21	963,0	18,13	83,3
20,80	428,1			65,51	1168,0	23,25	128,7
22,60	481,1			76,03	1361,0	28,39	201,0
24,60	541,1			86,93	1568,0	30,90	241,1
25,40	564,1			95,98	1763,0	32,99	277,8
				102,33	1966,0	34,42	326,5
				111,53	2178,0	38,31	373,7
				114,47	2373,0	38,04	409,8
						43,81	520,1
						46,83	579,8

Table 2.3 : The flow curves of the PEO solutions (0 to 100 ppm).

100 ppm (18,5°C)		50 ppm (19.5°C)		10 ppm (20°C)		solvent (19,5°C)	
$q_v\left(\frac{mm^3}{s}\right)$	P_g(mbar)	$q_v\left(\frac{mm^3}{s}\right)$	P_g(mbar)	$q_v\left(\frac{mm^3}{s}\right)$	P_g(mbar)	$q_v\left(\frac{mm^3}{s}\right)$	P_g(mbar)
4,30	7,1	2,42	3,9	2,47	4,1	2,54	4,0
5,23	9,1	3,73	6,1	5,05	8,2	5,23	8,1
6,31	12,7	4,82	8,0	7,46	12,0	7,88	12,1
8,60	19,1	5,98	9,9	9,60	16,1	10,40	16,2
9,82	23,5	7,05	11,9	11,44	19,8	12,88	19,9
10,70	25,0	9,36	15,7	20,08	39,8	24,80	39,1
11,30	30,8	11,20	22,0	27,52	59,4	36,00	60,3
12,60	33,6	10,16	20,5	40,08	97,2	13,92	18,1
13,90	41,1	15,28	41,0	55,84	145,0	27,20	38,9
15,10	50,7	19,04	61,5	68,08	193,0	38,64	59,1
16,00	54,9	26,08	102,0	93,60	288,0	54,40	93,4
17,10	63,9	33,60	146,0	114,40	386,0	76,64	151,0
20,00	79,6	44,56	204,0	155,20	581,0	92,80	195,0
21,90	91,8	75,68	403,0	187,20	778,0	151,20	394,0
23,30	99,8	105,60	604,0	220,00	948,0	190,40	583,0
30,40	150,0	135,20	804,0			122,40	296,0
34,90	195,0	160,80	984,0			232,00	782,0
45,90	291,0					258,40	938,0
63,40	405,0						
70,10	459,0						
83,20	606,0						
107,40	810,0						
122,60	950,0						

Table 2.5 : The flow curves of the 5000ppm PEO solution.

d=0.2 mm (21,5°C)				d=0.26 mm (20°C)			
$q_v\left(\frac{mm^3}{s}\right)$	P_g(mbar)	$q_v\left(\frac{mm^3}{s}\right)$	P_g(mbar)	$q_v\left(\frac{mm^3}{s}\right)$	P_g(mbar)	$q_v\left(\frac{mm^3}{s}\right)$	P_g(mbar)
0,98	4,9	15,5	495,0	12,2	25,0	45,5	1275,0
1,75	8,3	15,6	480,0	18,2	75,0	45,8	1175,0
2,51	10,2	16,1	526,0	22,9	125,0	49,5	1375,0
3,23	14,4	16,6	576,0	26,6	215,0	50,0	1275,0
4,27	19,3	16,9	591,0	27,2	275,0	52,8	1475,0
4,90	26,0	17,2	678,0	28,9	325,0	55,7	1575,0
5,76	28,6	18,2	944,0	29,2	215,0	58,1	1475,0
6,40	39,0	18,7	758,0	29,5	375,0	59,8	1675,0
6,72	38,2	19,1	944,0	31,3	475,0	62,2	1775,0
7,36	47,1	21,1	961,0	31,7	475,0	65,8	1675,0
7,40	50,1	26,4	1161,0	31,8	325,0	67,4	1875,0
8,16	63,1	29,7	1356,0	32,0	675,0	70,3	1975,0
8,30	65,1	32,1	1564,0	32,3	575,0	74,2	1875,0
9,08	94,0	34,6	1756,0	32,8	775,0	76,2	2075,0
9,20	87,1	37,2	1966,0	33,0	575,0	83,3	2275,0
9,33	86,1	40,0	2176,0	33,1	675,0	83,9	2075,0
9,52	105,0	42,8	2376,0	33,4	975,0	91,6	2275,0
9,79	101,1			34,0	775,0	118,3	2475,0
10,70	146,0			34,6	875,0	139,0	2675,0
10,90	141,0			34,8	475,0	142,5	2975,0
11,60	194,0			35,5	575,0	152,0	3475,0
11,70	181,0			36,1	975,0	152,9	2675,0
12,60	226,0			36,5	675,0	157,2	2875,0
13,20	285,0			37,4	775,0	172,9	2875,0
13,40	282,0			38,1	875,0	184,0	3975,0
13,90	332,0			39,0	1075,0	204,2	4975,0
14,40	386,0			39,2	1175,0	232,3	5975,0
14,50	381,0			39,7	975,0		
15,10	406,0			41,6	1175,0		
15,10	426,0			42,9	1075,0		

Table 2.6 : The flow curves of the PEO 1% solution. T=20°C.

d=0.2 mm		d=0.26 mm		d=0.53 mm	
$q_v\left(\frac{mm^3}{s}\right)$	P_g (mbar)	$q_v\left(\frac{mm^3}{s}\right)$	P_g (mbar)	$q_v\left(\frac{mm^3}{s}\right)$	P_g (mbar)
1,28	29,8	9,31	33,0	61,83	25,0
1,67	37,4	10,26	25,0	71,85	34,1
1,94	43,8	10,35	39,7	80,65	42,0
2,34	52,8	11,06	44,1	86,02	54,1
2,97	61,8	11,83	51,9	99,62	65,3
3,28	72,7	12,33	82,7	105,65	77,4
4,03	89,9	12,69	59,2	115,98	98,9
4,50	108,0	12,77	98,0	140,68	175,0
6,00	215,0	13,31	69,5	165,32	315,0
6,96	350,0	15,76	110,2	179,44	410,0
7,79	495,0	20,16	220,0	193,55	510,0
8,60	645,0	22,51	310,0	205,16	615,0
9,22	795,0	24,29	410,0	245,16	725,0
10,17	995,0	26,15	510,0	264,86	860,0
10,89	1195,0	27,34	610,0	284,27	1015,0
12,21	1500,0	30,56	808,0	309,68	1205,0
12,90	1650,0	33,69	1015,0	366,72	1510,0
14,25	1995,0	33,72	1740,0	393,15	1750,0
16,89	2495,0	35,71	1205,0	430,11	2005,0
19,09	2995,0	37,22	1505,0	496,28	2505,0
20,74	3485,0	44,09	2005,0	624,35	3010,0
22,47	3995,0	56,37	2512,0	664,71	3505,0
25,50	4505,0	66,50	3000,0	743,34	4015,0
30,02	4995,0	77,06	3530,0	819,80	4525,0
32,10	5520,0	79,57	3995,0	921,36	5005,0
34,80	5995,0	89,88	4490,0	1010,15	5505,0
49,85	7995,0	96,77	5010,0	1083,66	6005,0
		104,45	5490,0	1219,90	7005,0
		112,90	5990,0		

Table 2.7 : The flow curves of the PEO 4% solution. T=20°C.

d=0.2 mm		d=0.53 mm		d=1.2 mm	
$q_V\left(\frac{mm^3}{s}\right)$	P_g (mbar)	$q_V\left(\frac{mm^3}{s}\right)$	P_g (mbar)	$q_V\left(\frac{mm^3}{s}\right)$	P_g (mbar)
0,26	200,0	0,24	22,0	4,08	22,0
1,12	550,0	2,05	88,0	7,81	32,5
2,69	1030,0	3,77	126,0	11,28	43,5
3,58	1520,0	5,50	157,0	16,11	54,5
4,15	2000,0	9,93	240,0	22,22	68,5
4,30	2520,0	18,92	372,0	36,00	92,5
4,76	3500,0	20,96	419,0	49,12	105,5
4,84	3000,0	22,95	471,0	113,89	188,5
5,03	4450,0	24,50	507,0	151,67	250,5
5,03	4000,0	25,57	655,0	177,69	315,5
5,45	4970,0	26,64	767,0	316,44	501,5
5,98	5500,0	32,62	820,0	440,74	706,5
6,40	5970,0	36,04	951,0	580,25	1101,5
6,87	6500,0	40,54	1139,0	894,39	1746,5
7,50	7000,0	42,38	1350,0	1022,27	2386,5
8,11	7500,0	44,59	1320,0		
		48,99	1535,0		
		53,51	1850,0		
		54,81	1729,0		
		58,68	1922,0		
		63,34	2160,0		
		65,72	2830,0		
		65,79	2363,0		
		66,49	2320,0		
		77,67	3330,0		
		78,76	2820,0		
		82,33	3845,0		
		92,97	4337,0		
		113,31	4840,0		
		199,23	5810,0		

Table 2.8 : The flow curves of the PEO 10% solution. T=20°C.

d=0.2 mm		d=0.26 mm		d=0.53 mm		d=1.2 mm	
$q_V\left(\frac{mm^3}{s}\right)$	P_g(mbar)	$q_V\left(\frac{mm^3}{s}\right)$	P_g(mbar)	$q_V\left(\frac{mm^3}{s}\right)$	P_g(mbar)	$q_V\left(\frac{mm^3}{s}\right)$	P_g(mbar)
0,27	1,05	0,43	1,00	1,57	0,50	11,06	0,42
0,42	2,03	2,54	2,00	3,52	0,80	26,98	0,65
0,60	2,00	4,12	3,00	6,37	1,00	56,93	1,02
0,84	3,02	5,85	4,00	12,62	1,50	140,78	1,51
1,30	4,00	6,85	5,00	25,16	2,00	218,89	2,00
1,33	4,00	7,66	6,00	36,58	3,00		
1,74	5,00	7,90	7,00	48,39	4,00		
1,88	6,00	8,36	8,00	61,48	5,00		
1,97	6,00	8,96	9,00	67,56	6,00		
2,55	7,00	10,08	10,00	72,73	7,00		
2,63	8,00			76,21	8,00		
2,76	8,00			99,35	9,00		
3,03	9,00			119,41	10,00		
3,03	10,00			191,96	12,00		
3,47	10,00			300,33	14,00		
4,16	12,00			372,04	16,00		
4,47	12,00			470,97	18,00		
5,33	14,00			896,77	20,00		
5,96	15,00			1693,56	26,00		
7,71	16,00						
14,72	20,00						
14,89	19,00						
19,92	21,50						
38,33	26,00						
60,65	30,20						

Table 2.9 : The flow curve of the A1 solution. T=20°C.

d=0.26 mm (continued)							
$q_v\left(\frac{mm^3}{s}\right)$	P_g(mbar)	$q_v\left(\frac{mm^3}{s}\right)$	P_g(mbar)	$q_v\left(\frac{mm^3}{s}\right)$	P_g(mbar)	$q_v\left(\frac{mm^3}{s}\right)$	P_g(mbar)
0,00017	0,0338	0,0027	0,3186	0,0640	2,961	0,217	6,779
0,00025	0,0514	0,0028	0,2643	0,0677	3,315	0,234	7,196
0,00026	0,0579	0,0028	0,2778	0,0722	3,178	0,256	7,704
0,00029	0,0566	0,0029	0,3359	0,0795	3,990	0,275	8,054
0,00033	0,0625	0,0030	0,3517	0,0795	3,990	0,285	8,336
0,00038	0,0772	0,0030	0,2997	0,0812	3,423	0,287	8,558
0,00038	0,0691	0,0031	0,3139	0,0819	3,757	0,316	8,784
0,00045	0,0768	0,0032	0,3430	0,0850	4,101	0,393	11,439
0,00053	0,0857	0,0034	0,3846	0,0850	4,101	0,413	11,589
0,00062	0,0962	0,0034	0,4258	0,0860	3,699	0,426	16,000
0,00074	0,1085	0,0034	0,4139	0,0894	4,214	0,429	11,864
0,00084	0,1477	0,0035	0,3631	0,0894	4,214	0,451	12,216
0,00087	0,1231	0,0036	0,4067	0,0911	3,850	0,470	12,480
0,00103	0,1405	0,0037	0,4397	0,0939	4,304	0,491	12,696
0,00121	0,1610	0,0038	0,4198	0,0939	4,304	0,505	12,914
0,00138	0,2198	0,0040	0,4736	0,0957	4,147	0,517	13,373
0,00143	0,1852	0,0041	0,4318	0,0961	4,382	0,523	13,130
0,00152	0,2137	0,0043	0,4497	0,0961	4,382	0,596	13,835
0,00163	0,2108	0,0046	0,4641	0,0964	4,010	0,616	14,265
0,00166	0,2168	0,0047	0,4945	0,1019	4,178	0,621	13,619
0,00178	0,2230	0,0050	0,4813	0,1034	4,482	0,625	14,041
0,00185	0,3279	0,0052	0,4570	0,1034	4,482	0,645	14,550
0,00188	0,2889	0,0107	1,1385	0,1068	4,369	0,656	14,977
0,00193	0,2290	0,0135	1,3770	0,1081	4,565	0,686	14,793
0,00194	0,2259	0,0145	1,3177	0,1081	4,565	0,885	21,100
0,00204	0,2394	0,0151	1,4699	0,1107	4,653	1,138	26,200
0,00211	0,2476	0,0158	1,5065	0,1107	4,653	1,376	31,800
0,00212	0,2546	0,0163	1,4311	0,1116	4,752	1,716	39,100
0,00220	0,2548	0,0237	1,6724	0,1116	4,752	2,079	45,000
0,00227	0,2641	0,0361	2,2545	0,1150	4,521	3,039	64,900
0,00235	0,2728	0,0447	2,3090	0,1514	4,357	3,825	85,500
0,00244	0,2833	0,0503	2,5981	0,1696	5,601	4,321	97,800
0,00247	0,3569	0,0551	2,9081	0,1970	6,146	5,460	135,000
0,00251	0,2952	0,0567	2,7689	0,2129	6,622	5,880	800,000
0,00261	0,3053	0,0602	3,0820	0,2134	6,479	5,882	1200,00

d=0.26 mm (end)							
$q_v\left(\frac{mm^3}{s}\right)$	P_g(mbar)	$q_v\left(\frac{mm^3}{s}\right)$	P_g(mbar)	$q_v\left(\frac{mm^3}{s}\right)$	P_g(mbar)	$q_v\left(\frac{mm^3}{s}\right)$	P_g(mbar)
6,03	500,00	6,54	1800,00	7,11	2000,00	76,00	2020,00
6,07	1000,00	6,84	623,00	7,15	1520,00	78,40	2000,00
6,07	1500,00	6,90	420,00	13,68	2020,00	137,98	3020,00
6,39	228,00	6,95	1020,00	17,56	2000,00		
6,53	825,00	7,04	1220,00	64,65	2020,00		

Table 2.10 : The flow curve of the M1 fluid. T=21°C.

d=0.53 mm							
$q_v\left(\frac{mm^3}{s}\right)$	P_g(mbar)	$q_v\left(\frac{mm^3}{s}\right)$	P_g(mbar)	$q_v\left(\frac{mm^3}{s}\right)$	P_g(mbar)	$q_v\left(\frac{mm^3}{s}\right)$	P_g(mbar)
0,023	0,118	0,218	0,915	0,910	2,899	7,64	44,71
0,025	0,118	0,220	0,921	1,055	3,590	9,06	74,54
0,029	0,145	0,233	0,915	1,080	3,605	10,83	137,70
0,031	0,146	0,242	1,061	1,256	4,394	10,86	136,32
0,041	0,206	0,251	1,061	1,411	4,412	11,72	178,72
0,049	0,207	0,282	1,237	1,591	5,445	13,01	256,50
0,050	0,249	0,304	1,112	1,807	5,640	14,29	343,79
0,059	0,249	0,305	1,237	2,026	6,856	15,06	408,71
0,081	0,334	0,353	1,410	2,371	7,257	15,54	454,33
0,107	0,405	0,380	1,411	2,601	8,536	15,67	514,87
0,107	0,475	0,405	1,618	2,704	7,837	16,76	567,95
0,114	0,475	0,412	1,645	3,040	9,339	17,78	606,11
0,120	0,404	0,481	1,979	4,081	13,739	17,78	642,09
0,131	0,575	0,486	2,033	4,392	12,771	20,92	682,45
0,140	0,576	0,514	1,736	4,938	18,141	27,38	779,09
0,147	0,665	0,554	1,883	5,741	23,027	29,39	831,96
0,170	0,665	0,567	2,264	5,933	18,334	31,48	901,27
0,193	0,768	0,667	2,465	6,479	28,928	33,70	980,22
0,197	0,768	0,727	2,343	6,667	31,879	36,15	1063,35
0,207	0,723	0,825	2,953	6,778	33,727	36,48	1142,98

Table 2.11 : The flow curve of the pure PEO. T=100°C.

d=0.5mm	
$q_v\left(\frac{mm^3}{s}\right)$	P_g(mbar)
0,057	27,0
0,079	31,6
0,113	35,0
0,113	33,0
0,170	45,0
0,170	43,5
0,339	68,9
0,452	68,2
0,679	80,4
0,792	98,0
0,905	90,2
1,131	117,5
2,262	159,0
4,524	204,0
6,786	208,0
9,048	244,0
11,310	244,0
16,965	272,0
22,619	286,0
33,929	306,0

Table 2.12 : The shear viscosity of the PEO 4% solution at four different temperatures.

T = 26 °C		T = 23 °C		T = 20 °C		T = 17 °C	
$\dot{\gamma}(s^{-1})$	η (Pa.s)	$\dot{\gamma}(s^{-1})$	η (Pa.s)	$\dot{\gamma}(s^{-1})$	η (Pa.s)	$\dot{\gamma}(s^{-1})$	η (Pa.s)
0,097	151,3	0,087	157,4	0,090	176,2	0,087	213,5
0,106	148,3	0,094	155,9	0,094	177,5	0,090	217,5
0,111	149,4	0,100	156,7	0,099	178,7	0,096	214,7
0,190	139,0	0,104	159,6	0,101	182,3	0,099	218,4
0,299	121,2	0,175	151,5	0,113	171,6	0,106	212,9
0,440	104,4	0,269	134,7	0,116	175,0	0,109	216,3
0,612	91,1	0,395	116,5	0,139	171,5	0,114	214,0
0,831	78,9	0,548	101,8	0,142	174,2	0,170	201,3
1,074	70,1	0,744	88,1	0,194	163,0	0,256	172,0
1,363	62,4	0,964	78,1	0,285	142,3	0,347	152,0
1,746	54,9	1,226	69,4	0,387	127,2	0,469	133,5
2,104	49,3	1,514	62,6	0,518	112,2	0,615	117,7
2,530	44,8	1,872	55,9	0,622	104,7	0,787	104,4
3,056	40,3	2,281	50,2	0,754	95,7	0,985	93,3
3,628	36,7	2,718	45,7	0,891	88,9	1,213	83,9
4,214	33,9	3,239	41,4	0,978	84,5	1,480	75,3
4,956	30,8	3,814	37,7	1,064	81,0	1,506	74,7
5,756	28,2	4,454	34,5	1,267	73,6	1,828	66,9
5,823	28,0	5,157	31,7	1,461	68,6	1,848	66,7
5,890	27,9	5,892	29,4	1,685	63,7	1,896	65,5
5,956	27,7	6,052	28,9	1,916	59,7	2,259	59,3
6,062	27,4			2,192	55,4	2,279	59,2
						2,561	55,3
						2,597	55,0
						3,042	50,1
						3,566	45,5
						3,779	44,0
						3,985	42,7

Table 2.13 : The shear viscosity of PEO solutions at 20°C.

c = 5000 ppm		c = 1%		c = 10%	
$\dot{\gamma}(s^{-1})$	η (Pa.s)	$\dot{\gamma}(s^{-1})$	η (Pa.s)	$\dot{\gamma}(s^{-1})$	η (Pa.s)
0,036	0,250	0,200	0,631	0,001	4670,0
0,062	0,219	0,132	0,677	0,002	5000,0
0,091	0,224	0,097	0,646	0,004	4775,0
0,149	0,213	0,166	0,668	0,006	4550,0
0,244	0,225	0,212	0,680	0,010	4550,0
0,269	0,232	0,304	0,644	0,030	3333,3
0,282	0,228	0,401	0,634	0,060	2616,7
0,439	0,226	0,521	0,633	0,100	2130,0
0,718	0,220	0,676	0,634	0,300	1186,7
1,117	0,220	0,951	0,612	0,600	763,3
1,738	0,222	1,346	0,613	1,000	498,0
2,841	0,209	1,885	0,594	4,000	167,5
4,420	0,197	2,532	0,600	10,000	85,3
7,224	0,183	3,311	0,596	30,000	36,7
11,240	0,173	4,721	0,567	60,000	21,1
17,490	0,162	6,227	0,558		
27,220	0,150	8,765	0,538		
40,320	0,138	12,450	0,514		
62,730	0,129	18,960	0,479		
92,930	0,122	31,140	0,431		
118,800	0,119	45,850	0,398		
144,600	0,114	65,000	0,364		
167,600	0,112	103,300	0,325		
300,000	0,103	156,300	0,291		
600,000	0,094	250,200	0,258		
1000,000	0,089	407,500	0,225		
		609,300	0,204		
		768,100	0,192		
		972,800	0,181		

Table 2.14 : The shear viscosity of the PIB solutions.

M1		M1		M1		A1	
T = 20°C		T = 23°C		T = 26°C		T = 20°C	
$\dot{\gamma}(s^{-1})$	η (Pa.s)	$\dot{\gamma}(s^{-1})$	η (Pa.s)	$\dot{\gamma}(s^{-1})$	η (Pa.s)	$\dot{\gamma}(s^{-1})$	η (Pa.s)
0,057	3,706	0,115	2,953	0,103	2,186	0,063	19,640
0,109	3,654	0,223	2,868	0,166	2,158	0,103	17,140
0,195	3,591	0,453	2,681	0,269	2,119	0,126	16,830
0,332	3,478	0,871	2,639	0,430	2,113	0,178	14,930
0,407	3,454	1,684	2,584	0,682	2,119	0,264	13,420
0,544	3,508	3,071	2,532	1,094	2,100	1,323	6,680
0,917	3,441	5,334	2,458	1,747	2,092	6,800	2,600
1,123	3,345	9,281	2,382	2,847	2,043	20,000	1,320
1,541	3,381	16,470	2,264	4,629	1,999	30,000	1,010
2,618	3,288			11,520	1,812	120,000	0,442
3,099	3,239					370,300	0,239
4,400	3,232					951,300	0,130
7,660	3,067					1000,000	0,137
8,639	3,107						
13,140	2,955						
21,940	2,922						
23,880	3,005						